

# Strengthening Mechanisms and Their Relative Contributions to the Yield Strength of Microalloyed Steels

JUNFANG LU, OLADIPO OMOTOSO, J. BARRY WISKEL, DOUGLAS G. IVEY,  
and HANI HENEIN

Microalloyed steels are used widely in oil and gas pipelines. They are a class of high-strength, low-carbon steels that contain small additions (in amounts less than 0.1 wt pct) of Nb, Ti, and/or V. The steels may contain other alloying elements, such as Mo, in amounts exceeding 0.1 wt pct. Precipitation in these steels can be controlled through thermomechanical-controlled processing, leading to precipitates with sizes that range from several microns to a few nanometers. Microalloyed steels have good strength, good toughness, and excellent weldability, which are attributed in part to the presence of the nanosized carbide and carbonitride precipitates. Because of their fine sizes, wide particle size distribution, and low volume fractions, conventional microscopic methods are not satisfactory for quantifying these precipitates. Matrix dissolution is a promising alternative to extract the precipitates for quantification. Relatively large volumes of material can be analyzed so that statistically significant quantities of precipitates of different sizes are collected. In this article, the microstructure features of a series of microalloyed steels (X70, X80, and X100) as well as a Grade 100 steel are characterized using optical microscopy (OM) and scanning electron microscopy (SEM). A chemical dissolution technique is used to extract the precipitates from the steels. Transmission electron microscopy (TEM) and X-ray diffraction (XRD) are combined to analyze the chemical composition of these precipitates. Rietveld refinement of the XRD patterns is used to quantify fully the relative amounts of these precipitates. The size distribution of the nanosized precipitates is quantified using dark-field imaging (DF) in the TEM. The effects of microalloying content, finish rolling temperature (FRT), and coiling temperature (CT)/interrupted cooling temperature (ICT) on the grain size and the amount of nanoprecipitation are discussed. Individual strengthening contributions from grain size effects, solid-solution strengthening, and precipitation strengthening are quantified to understand fully the strengthening mechanisms for these steels.

DOI: 10.1007/s11661-012-1135-3

© The Minerals, Metals & Materials Society and ASM International 2012

## I. INTRODUCTION

THE addition of microalloying additives, such as Nb, Ti, and V, to steels combined with thermomechanical controlled processing (TMCP) can enhance the strength and ductility of steel. The improvement of mechanical properties results mainly from the refinement of ferrite grain size, precipitation, solid-solution strengthening, and dislocation strengthening.<sup>[1–3]</sup> The first three can be expressed by Eq. [1]. Dislocation strengthening is not included in Eq. [1] because cold deformation is not used commonly in hot-rolled or normalized microalloyed steels.<sup>[3]</sup>

$$\sigma_{ys}(\text{MPa}) = \sigma_i + k_y d^{-1/2} + \left( \frac{10.8 v_f^{1/2}}{X} \right) \ln \left( \frac{X}{6.125 \times 10^{-4}} \right) + \sum k_i C_i \quad [1]$$

where  $\sigma_{ys}$  is the yield stress,  $\sigma_i$  is the friction stress of iron,  $k_y$  is the strengthening coefficient for grain size,  $d$  is the grain diameter in microns,  $X$  is the size of precipitates in microns,  $v_f$  is the volume fraction of a given precipitate size ( $X$ ),  $k_i$  is the strengthening coefficient for solute strengthening of solute  $i$ , and  $C_i$  is the concentration of solute  $i$ .

The TMCP schedule is illustrated in Figure 1, and it includes the following steps<sup>[1]</sup>:

- Reheating the steel to a selected temperature to dissolve many of the microalloyed precipitates (with the notable exception of TiN, which may only partially dissolve) in the steel.
- Rough rolling at temperatures above the no-recrystallization temperature ( $T_{nr}$ ) to break down the austenite grains through multiple recrystallization cycles.
- Finish rolling at temperatures below  $T_{nr}$  but above the austenite to ferrite transformation temperature ( $A_{r3}$ ), to produce heavily pancaked austenite.

JUNFANG LU, Engineer, is with the Enbridge Pipelines Inc., Edmonton, AB T5J 3N7, Canada. OLADIPO OMOTOSO, Research Engineer, is with the Suncor Energy Inc., Fort McMurray, AB T9H 3E3, Canada. J. BARRY WISKEL, Research Associate, and DOUGLAS G. IVEY and HANI HENEIN, Professors, are with the Department of Chemical and Materials Engineering, University of Alberta, Edmonton, AB T6G 2V4, Canada. Contact e-mail: doug.ivey@ualberta.ca

Manuscript submitted June 16, 2011.

Article published online March 29, 2012

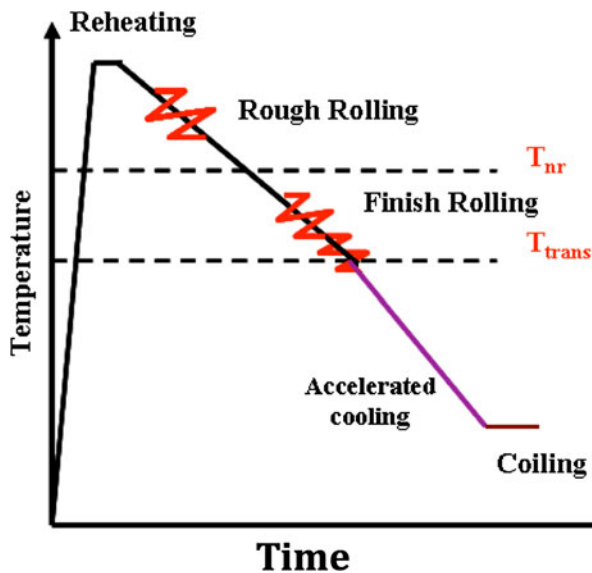


Fig. 1—Schematic of a thermomechanical-controlled processing (TMCP) schedule.

- (d) Accelerated cooling from a temperature above  $A_{r3}$  down to a temperature at which the desired stable microstructure can be obtained.
- (e) Slow cooling of the coil, during which fine precipitates are formed.

Precipitation occurs during TMCP. It is a complex process because it takes place within the steel matrix and the matrix itself is evolving continuously from the austenite to ferrite. Many factors affect the precipitation of nanoprecipitates, such as steel chemistry, processing histories, strain, *etc.*

Different sized precipitates have been identified in microalloyed steels, such as large TiN precipitates that are several microns in size and Nb-rich precipitates less than 5 nm in size. Intermediate-size Ti/Nb precipitates have been observed as well.<sup>[4]</sup> The size difference among these precipitates is caused by their different formation temperatures and solubility. Figure 2<sup>[3]</sup> shows a comparison of the solubility products (*e.g.*, for NbC,  $K_s = [\text{Nb}]_{\text{equilibrium}}[\text{C}]_{\text{equilibrium}} = 10^{(A-B/T)}$ , where  $K_s$  is the solubility product,  $T$  is the temperature in Kelvin, and  $A$  and  $B$  are constants for a given system) for various microalloyed carbides and nitrides. It is clear that TiN is the least soluble of the precipitates in austenite. TiN is expected to precipitate out at higher temperatures during initial processing stages leading to its large size. NbC has a much higher solubility in austenite and will precipitate out at lower temperatures during the later processing stages, producing particles with a much smaller size. Therefore, the solubility of the precipitates establishes guidelines to identify different phases. According to the precipitate size and their precipitation sequence, the precipitates can be classified into different groups.

The precipitates of different sizes contribute to steel strengthening in various ways. The precipitates formed in austenite during hot rolling have grain refinement effects on the austenite. These precipitates include the carbides, nitrides, and/or carbonitrides of Nb and Ti,

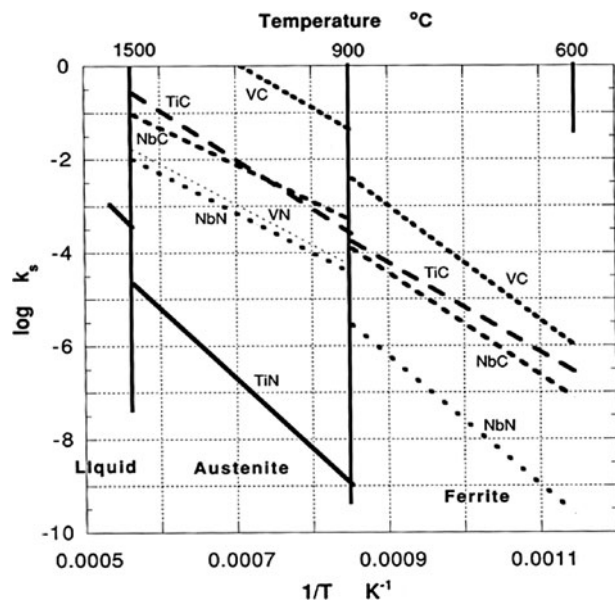


Fig. 2—Equilibrium solubility products for microalloyed carbides and nitrides in austenite and ferrite.<sup>[3]</sup>

which are larger than 20 nm in size.<sup>[5,6]</sup> Fine particles (<20 nm), especially those smaller than 5 nm, contribute to precipitation strengthening. Precipitation strengthening effects are related closely to the precipitate volume fraction and size; more specifically, precipitation strengthening increases as the volume fraction of the precipitates increases and the precipitate size decreases.<sup>[1]</sup>

To enhance the precipitation strengthening effect, it is critical to refine the precipitate size and increase the volume fraction of the resulting nanoprecipitates. As such, the determination of the volume fraction of the nanoprecipitates is a priority, which is a goal of this article, *i.e.*, to combine different techniques to quantify the volume fraction of nanoprecipitates in microalloyed steels. However, this process is challenging because of the fine particle sizes, wide particle size distribution, and low volume fractions of the precipitates. The Ti and Nb carbonitrides have the same crystal structure (NaCl-type) and similar lattice parameters, making it difficult to differentiate the precipitates using X-ray diffraction (XRD).

Because of the limited resolution and/or sample size, conventional microscopic methods, such as optical microscopy and electron microscopy (both scanning electron microscopy [SEM] and transmission electron microscopy [TEM] coupled with energy-dispersive X-ray spectroscopy and electron diffraction), are not completely satisfactory for precipitate quantification, particularly volume fractions of fine precipitates.<sup>[4]</sup> Researchers have used thermodynamic modelling to explore the equilibrium conditions and phase relationships in complex alloys. Guo and Sha<sup>[7]</sup> have used JMatPro (acronym for Java-based Materials Properties; Sente Software Ltd., Guildford, U.K.) to calculate the precipitate type and equilibrium fraction for Al-Si-Cu

alloys. The precipitate  $\text{Al}_2\text{Cu}$  fraction is estimated based on an X-ray diffraction analysis. Prat *et al.*<sup>[8]</sup> have estimated the volume fraction of MX (Ta(C,N) and V(C,N)) and  $\text{M}_{23}\text{C}_6$  precipitates with Thermo-Calc Software (Stockholm, Sweden). Zavaleta *et al.*<sup>[9]</sup> studied MX precipitate phases (M = Nb, V, Ti; X = C, N). Thermodynamic calculations on equilibrium phase relationships were performed using CALPHAD with Thermo-Calc.

Based on previous research work by the authors,<sup>[4,10]</sup> matrix dissolution provides a feasible alternative. Relatively large volumes of material are analyzed by matrix dissolution, from which statistically significant quantities of precipitates of different sizes are collected. The steel samples as well as the collected precipitates are more representative of the steel strip than the limited sample sizes used in conventional transmission electron microscopy studies.

In the current work, matrix dissolution was done chemically using HCl to extract Ti and Nb carbonitrides. The precipitates were separated from the solution by centrifuging. The extracted precipitates were identified using TEM and XRD without interference from the matrix. The precipitate size was characterized through TEM imaging, and the chemistry was determined by TEM X-ray microanalysis. Rietveld refinement of XRD patterns was used to obtain the relative precipitate abundance, from which the precipitate volume fraction was determined. Based on the volume fraction and the size of the nanoprecipitates, the precipitation strengthening effects for several steels were obtained. Other individual strengthening contributions from the grain size effect and solid solution strengthening were quantified as well in an attempt to correlate strengthening fully with the microstructure. The effects of microalloy composition, finish rolling temperature (FRT), and coiling temperature (CT)/interrupted cooling temperature (ICT) on the grain size and the amount of nanoprecipitates are discussed. This approach was applied to four grades of microalloyed steels, Grade100, X70, X80, and X100. For Grade100 steel, the designation is the strength equivalent of Canadian Standards Association (CSA) Grade 690. It has a specified minimum yield strength (SMYS) of 100 ksi (690 MPa). X70, X80, and X100 steels are designated based on American Petroleum Institute (API) specifications. The number refers to the SMYS in ksi.

## II. EXPERIMENTAL PROCEDURE

### A. Chemical Composition, Processing Histories, and Mechanical Properties of Steels

The four grades of microalloyed steels, Grade100, X70, X80, and X100, were supplied by EVRAZ Inc. NA (Chicago, IL). Grade100 microalloyed steel is a high-strength, low-alloy structural steel. It has the highest amount of microalloying elements (Nb + Ti + V) of the steels studied, so it is expected to have more precipitates than the other steels. The X70, X80, and X100 steels are intended for production of oil and gas transmission pipelines. The X70 steel is currently the most widely used for this purpose, whereas the X80 steel will find increasing application in the near future. The X100 steel is a newer steel for future development. All these steel grades are produced commercially except for X100. The X100 steels used in this study were experimental steels. The combination of these steels (from X70 to X100 and Grade100) allows for the exploration of the differences in chemistry and processing that affect the mechanical properties. Several steels are at the same strength level designation (four X80 steels and three X100 steels). Including these steels provides some insight into how differences in processing and composition can give rise to the same mechanical properties.

The steel chemical compositions and processing histories, namely the FRT and the CT/ICT, as well as the mechanical properties, are given in Tables I and Table II.<sup>[11]</sup>

The respective FRT and CT/ICT temperatures for the X80-B4F steel were used as the base values. The corresponding temperatures for the other steels are normalized with respect to this steel in Table II. Although only relative processing temperatures are provided in this article, the results are sufficiently clear at to show trends related to the principle alloying elements in these commercial grades that are extensions of the model steel alloys.

### B. Steel Microstructure Analysis and Grain Size Measurement

The steel specimens were polished and etched with 2 pct Nital for microstructural observation and grain size measurement. The exposed sample surface was through the pipe/plate thickness and perpendicular to

Table I. Chemical Composition (wt pct) for Microalloyed Steels<sup>[7]</sup>

Sample ID	C	Mn	Si	Al	N	Cu + Ni + Cr	Mo	Nb	Ti	V	B (ppm)
Grade100	0.080	1.800	0.244	0.05	0.011	0.877	0.301	0.094	0.060	0.047	—
X70-564	0.0398	1.654	0.23	0.022	0.0118	0.432	0.2	0.069	0.023	0.001	—
X80-462	0.03	1.69	0.27	0.044	0.0098	0.45	0.297	0.091	0.013	0.002	—
X80-A4B	0.035	1.7	0.283	0.044	0.0058	0.66	0.305	0.094	0.017	0.003	—
X80-B4F	0.052	1.62	0.128	0.02	0.0061	0.62	0.299	0.077	0.009	0.002	—
X80-A4F	0.052	1.77	0.115	0.016	0.0055	0.64	0.404	0.044	0.009	0.003	—
X100-2A	0.039	1.81	0.11	0.018	0.0050	0.98	0.41	0.037	0.013	0.003	11
X100-2B	0.065	1.87	0.22	0.032	0.0059	0.77	0.40	0.047	0.009	0.070	1
X100-3C	0.064	1.88	0.33	0.024	0.0063	0.74	0.40	0.046	0.009	0.003	—

**Table II. Processing Histories and Mechanical Properties for Microalloyed Steels<sup>17</sup>**

Sample ID	Type	FRT (K/K)	CT (K/K)	ICT (K/K)	CR (K/s)	$\sigma_{ys}$ (MPa)	$\sigma_{UT}$ (MPa)
Grade100	plate	1.05		1.06	15	788	928
X70-564	pipe	0.96	1.03		15	520	650
X80-462	pipe	0.96	1.03		15	588	703
X80-A4B	pipe	1.04	0.95		15	568	694
X80-B4F	pipe	1.00	1.00		15	592	735
X80-A4F	pipe	1.00	0.93		15	589	717
X100-2A	plate	1.00		0.80	35	810	907
X100-2B	plate	1.00		0.75	34	691	793
X100-3C	plate	1.00		0.87	19.1	744	846

CR, nominal cooling rate.

the rolling direction. A JSM6301 (JEOL Ltd., Tokyo, Japan) field-emission source SEM was used to take secondary electron (SE) images for steel grain size measurement. The SEM was operated at a relatively low accelerating voltage, *i.e.*, 5 kV, for better surface resolution. The images were taken within 1/8 to 3/8 of the pipe/plate thickness for grain size measurement.

Because the grains are nonequiaxed, *i.e.*, they are highly irregular in shape, a variation on the standard ASTM technique was used for the grain size measurement. Mean linear intercepts (*m.l.i.*) were used to measure the grain size, as shown in Figure 3. The lines (horizontal, vertical, and at 45 deg and 135 deg, three of each) were drawn, and the number of grains (grain boundaries) intersected by each line was counted. The ratio of the line length (*l*) to the number of grains (*n*) provided an estimation of the grain size ( $\bar{d} = l/n$ ). At least three SEM images per sample were analyzed; the minimum area analyzed was 5000  $\mu\text{m}^2$ . Approximately 240 grains for the X-70 steel and 350 grains for the X80 steels were measured. The standard deviation was obtained from the preceding measurements.

### C. Precipitate Extraction and Characterization

Chemical dissolution was used for all steels to extract the Ti and Nb carbonitride precipitates using an HCl acid solution at 338 K to 343 K (65 °C to 70 °C) (1:1 mixture by volume of HCl acid, with a specific gravity of 1.19, and distilled water). After the steel matrix was dissolved, a Sorvall RC-6 superspeed centrifuge (Mandel Scientific Co., Guelph, Ontario, Canada), was used to separate the solid particles from the solution by rotating the material rapidly at up to 40,000 RCF (relative centrifugal force) at 277 K (4 °C). The centrifuging process was repeated several times to clean the precipitates. Inductively coupled plasma (ICP) spectroscopy, with a PerkinElmer Elan 6000 ICP-MS (PerkinElmer, Waltham, MA), was used to analyze the concentration of the elements in the supernatant extracted by HCl dissolution, as a means of performing a mass balance. An analytical balance with an accuracy of 0.1 mg was used to measure the weight of the sample before dissolution and the weight of the extracted residues. The typical amounts of steel dissolved were 20 g and the extracted residue was approximately 150 mg.

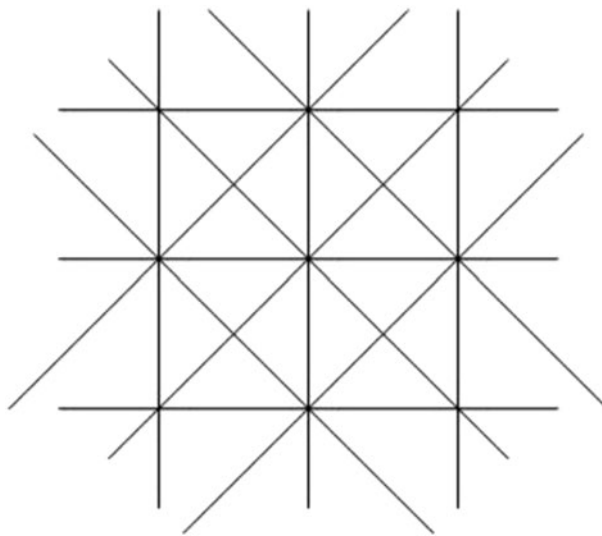


Fig. 3—Schematic showing line pattern used for grain size measurement via the mean linear intercept method.

The residues extracted by matrix dissolution were used for phase identification using TEM. To prepare TEM samples from the extracted residue, a fraction of the extracted residue was dispersed in ethanol and then a drop of the suspension was deposited on a carbon-coated, 300-mesh Cu grid. The solvent was allowed to evaporate, leaving behind the particles. The compositions of the various precipitates were determined by energy-dispersive X-ray analysis (EDX) in the TEM, where a standardless approach was used. The TEM samples prepared in this manner produced many precipitates. However, amorphous  $\text{SiO}_2$  was present in the residue, which interfered with the nanoprecipitate size distribution analysis. This process has been explained elsewhere.<sup>[4,10]</sup>

To quantify nanoprecipitate size distribution, another type of sample was used for TEM analysis: extracted carbon replicas. The carbon replicas were prepared by etching the matrix of a polished steel sample selectively, evaporating a thin layer of carbon onto the etched surface, and then lifting the carbon layer containing precipitates from the surface and supporting on a 300-mesh Cu grid. Dark-field (DF) imaging in the TEM was used to characterize the size distribution of the extracted



nanoprecipitates on the carbon replicas. The precipitates extracted through the carbon replicas did not contain any of the amorphous SiO<sub>2</sub> particles obtained during matrix dissolution, which made the precipitate size distribution analysis easier to perform. All the TEM samples were examined in a JEOL 2010 TEM, equipped with an EDX detector, operating at 200 kV.

The extracted residues from HCl dissolution were also analyzed using XRD, with a Bruker D8 advance X-ray diffractometer (Bruker AXS, Madison, WI) equipped with a Co X-ray source and a VANTEC-1 linear detector (Vantec Thermal Technologies, Fremont, CA). A fixed 0.3 deg divergent slit was used for all samples. TOPAS Academic software (Brisbane, Australia) was used for quantitative Rietveld analysis of the precipitate XRD patterns to determine the relative amounts of the various precipitates. The technique uses a nonlinear least-squares method to refine the instrument and structural parameters contributing to a calculated diffraction pattern until a good match is generated.<sup>[12,13]</sup> Given that the precipitates have similar structures and lattice parameters, the element occupancies were fixed based on the precipitate chemical composition obtained by EDX analysis in the TEM. The scale factor and lattice parameters (with tight restraints) were refined to reduce the strong parameter

correlations. The weight fraction for a given phase was determined using Eq. [2].<sup>[14]</sup>

$$w_a = \frac{SF_a(MZV)_a}{\sum_j SF_j(MZV)_j} \quad [2]$$

where  $w_a$  is the relative weight fraction of phase  $a$  in a mixture of  $j$  phases,  $SF$  is the refined scale factor which is proportional to the number of unit cells of phase  $a$  in the specimen,  $M$  is the mass of the molecular formula,  $Z$  is the number of formula units per unit cell, and  $V$  is the volume of the unit cell.

### III. RESULTS

#### A. Grain Size Measurement

The SEM SE images for the various steels are given in Figure 4. Grade100 steel is composed primarily of bainitic ferrite and smaller amounts of polygonal ferrite.<sup>[4]</sup> The basic microstructures of the X70 and X80 steels are similar, *i.e.*, coarse polygonal ferrite.<sup>[4]</sup> The X100 steels all have a similar microstructure, *i.e.*, acicular or bainitic ferrite with a few dispersed martensite and retained austenite islands.<sup>[4]</sup> Figure 5 shows the measured *m.l.i.* for all the steels studied. The ferrite

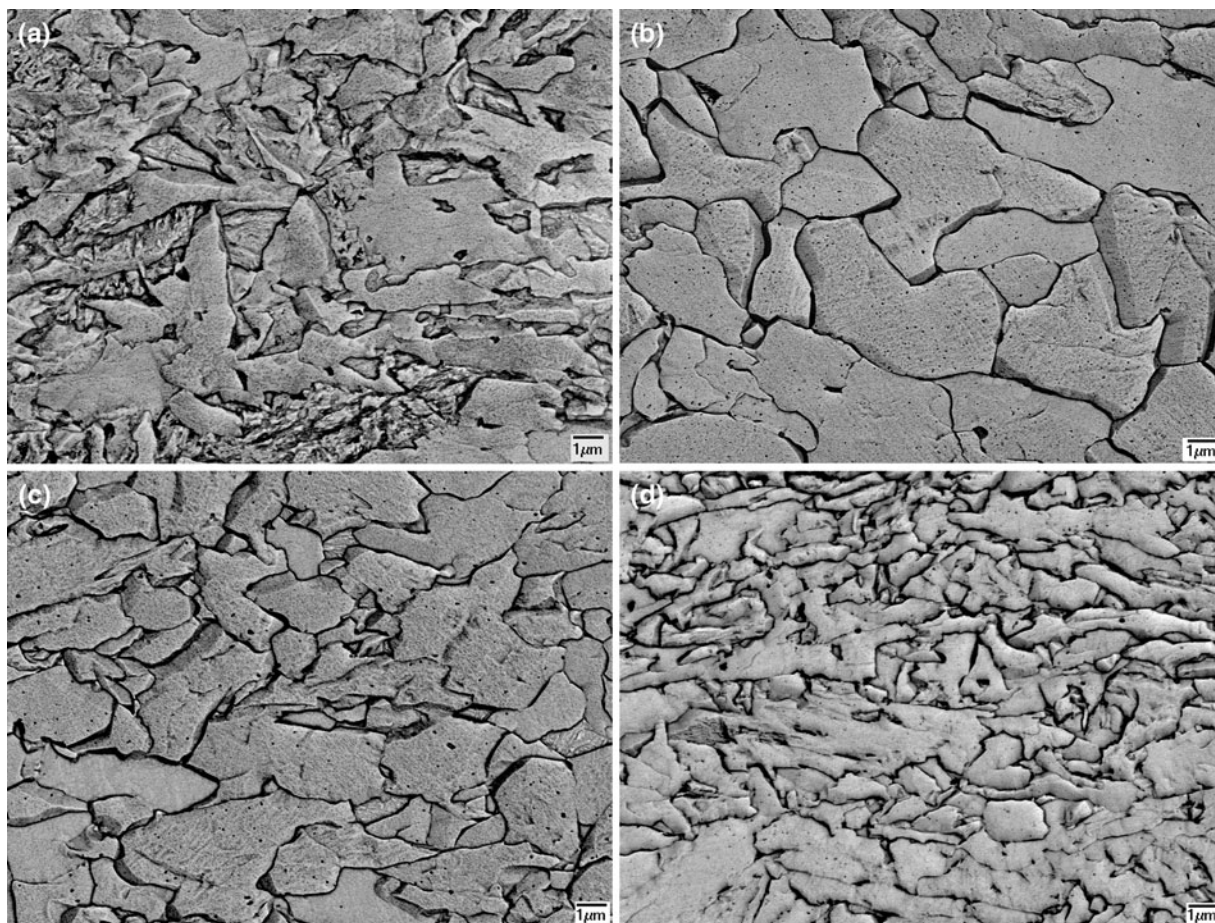


Fig. 4—Inverted SE-SEM images of microalloyed steels for grain size measurement, using an accelerating voltage of 5 kV: (a) Grade100 steel; (b) X70-567; (c) X80-462; and (d) X100-2B.

grain size decreases generally with an increasing steel grade; this effect is related to the processing histories, specifically CR and CT/ICT.

**B. Mass Balance of the Supernatant and the Extracted Residue Determined from Matrix Dissolution**

After the precipitates were extracted from the solution, ICP analysis was performed on the supernatant for all the steels studied. By comparing the chemical composition of the steel with the ICP results, the amount of each element extracted from the steel as part of the residue was obtained, as shown in Table III.

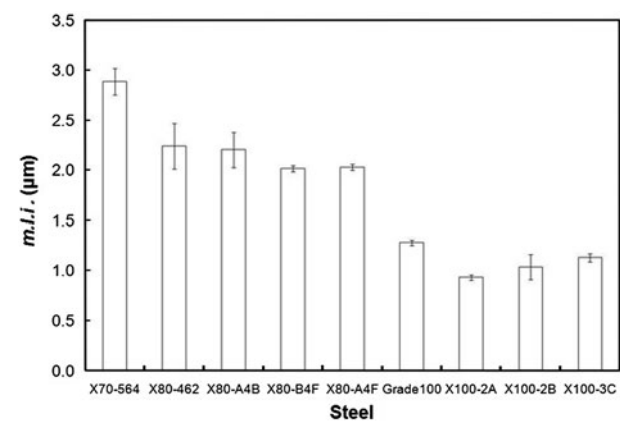


Fig. 5—Summary of mean linear intercept (*m.l.i.*) measurements.

Note that the percentage of a microalloying element that ends up in a precipitate particle in these steels is termed the extraction yield. The supernatant chemistry for a given element is defined as the mass of that element in the supernatant per unit mass of steel being dissolved, expressed as a wt pct. Most of the Si in the steel matrix and inclusions was collected in the residue as amorphous SiO<sub>2</sub>, as explained elsewhere.<sup>[10]</sup> Most of the Nb in the steel was in precipitate form, and the Nb extraction yield was between 68 pct and 97 pct. Lower yields were found for Ti, Mo, and V, especially for Mo and V. The extraction yield was below 21 pct for Mo; the V yield was below 5 pct for Grade100 and X100-2B. Most of the Mo and V was dissolved in the ferrite matrix.

**C. TEM Characterization of Extracted Residues**

The precipitates extracted from Grade100 steel by HCl dissolution and through carbon replicas have been discussed elsewhere, in terms of precipitate type and size distributions.<sup>[10]</sup> A similar TEM analysis was applied to all the other steels. Based on TEM-EDX microanalysis and TEM imaging, the average compositions, composition ranges (expressed as a standard deviation), and sizes of the precipitates were obtained. The precipitates can be categorized into different groups for all steels, but with some chemistry variations. Table IV shows the precipitate groupings for the Grade100, X70, and X80 steels according to their chemistry and size.

An example is given for Grade100 steel, where Ti-rich (two types), Ti/Nb-rich, Nb-rich, and nanoprecipitates

**Table III. ICP Analysis of the Supernatant from the Microalloyed Steels by HCl Dissolution**

Steel	Element	Si	Nb	Ti	Mo	V
Grade100	steel chemistry (wt pct)	0.244	0.094	0.06	0.301	0.047
	supernatant chemistry (wt pct)	0.021	0.003	0.014	0.257	0.045
	extraction yield of precipitates	91.6 pct	97.2 pct	76.3 pct	14.5 pct	5.0 pct
X70-564	steel chemistry (wt pct)	0.23	0.069	0.023	0.2	N/A
	supernatant chemistry (wt pct)	0.029	0.013	0.018	0.159	N/A
	extraction yield of precipitates	87.2 pct	81.0 pct	22.7 pct	20.3 pct	N/A
X80-462	steel chemistry (wt pct)	0.27	0.091	0.013	0.297	N/A
	supernatant chemistry (wt pct)	0.019	0.004	0.007	0.273	N/A
	extraction yield of precipitates	93.0 pct	96.0 pct	48.0 pct	8.1 pct	N/A
X80-A4B	steel chemistry (wt pct)	0.283	0.094	0.017	0.305	N/A
	supernatant chemistry (wt pct)	0.017	0.016	0.002	0.271	N/A
	extraction yield of precipitates	93.9 pct	82.9 pct	88.3 pct	11.3 pct	N/A
X80-B4F	steel chemistry (wt pct)	0.128	0.077	0.009	0.299	N/A
	Supernatant chemistry (wt pct)	0.017	0.005	0.003	0.273	N/A
	extraction yield of precipitates	86.5 pct	93.7 pct	69.7 pct	8.6 pct	N/A
X80-A4F	steel chemistry (wt pct)	0.115	0.044	0.009	0.404	N/A
	supernatant chemistry (wt pct)	0.014	0.009	0.004	0.394	N/A
	extraction yield of precipitates	87.7 pct	79.5 pct	59.2 pct	2.6 pct	N/A
X100-2A	steel chemistry (wt pct)	0.11	0.037	0.013	0.41	N/A
	supernatant chemistry (wt pct)	0.02	0.012	0.007	0.407	N/A
	extraction yield of precipitates	81.4 pct	68.1 pct	48.2 pct	0.8 pct	N/A
X100-2B	steel chemistry (wt pct)	0.22	0.047	0.009	0.40	0.07
	supernatant chemistry (wt pct)	0.021	0.013	0.004	0.399	0.069
	extraction yield of precipitates	90.4 pct	73.0 pct	52.9 pct	0.4 pct	2.0 pct
X100-3C	steel chemistry (wt pct)	0.33	0.046	0.009	0.40	N/A
	supernatant chemistry (wt pct)	0.019	0.008	0.001	0.397	N/A
	extraction yield of precipitates	94.3 pct	75.0 pct	88.2 pct	0.8 pct	N/A

N/A, not applicable.

**Table IV. Classification of Precipitates for Grade100, X70, and X80 Steels According to Composition and Size (from Rietveld Refinements of XRD Patterns and TEM)**

Steel	Mean Precipitate Chemistry	Lattice Parameter (nm)	Standard Deviation of Composition in Atomic Fraction			Size (nm)
			Ti	Nb	Mo	
Grade100	Ti <sub>0.9</sub> Nb <sub>0.1</sub> N	0.4250	0.05	0.05	N/A	300 to 3000
	Ti <sub>0.77</sub> Nb <sub>0.23</sub> C <sub>0.5</sub> N <sub>0.5</sub>	0.4282	0.05	0.05	N/A	100 to 300
	Ti <sub>0.5</sub> Nb <sub>0.5</sub> C <sub>0.5</sub> N <sub>0.5</sub>	0.4329	0.07	0.07	N/A	100 to 200
	Nb <sub>0.7</sub> Ti <sub>0.3</sub> C <sub>0.5</sub> N <sub>0.5</sub>	0.4419	0.05	0.05	N/A	100 to 200
X70-564	Nb <sub>0.48</sub> Mo <sub>0.28</sub> Ti <sub>0.21</sub> V <sub>0.03</sub> C	0.439*	0.07	0.07	0.03	≤10, spherical
	Ti <sub>0.70</sub> Nb <sub>0.25</sub> Mo <sub>0.05</sub> N	not in XRD	0.02	0.03	0.01	60 to 100
	Nb <sub>0.52</sub> Ti <sub>0.43</sub> Mo <sub>0.05</sub> C <sub>0.5</sub> N <sub>0.5</sub>	0.4436	0.13	0.11	0.03	20 to 40
	Nb <sub>0.79</sub> Ti <sub>0.15</sub> Mo <sub>0.06</sub> C <sub>0.5</sub> N <sub>0.5</sub>	0.4437	0.06	0.06	0.03	20 to 40
X80-462	Nb <sub>0.58</sub> Mo <sub>0.42</sub> C	0.440*	N/A	0.03	0.03	≤10, spherical
	Ti <sub>0.76</sub> Nb <sub>0.24</sub> N	0.4261	0.05	0.05	N/A	100 to 200
	Ti <sub>0.55</sub> Nb <sub>0.45</sub> C <sub>0.5</sub> N <sub>0.5</sub>	0.4336	0.10	0.10	N/A	80 to 100
	Nb <sub>0.86</sub> Ti <sub>0.14</sub> C <sub>0.5</sub> N <sub>0.5</sub>	0.4434	0.04	0.04	N/A	40 to 90
X80-A4B	Nb <sub>0.8</sub> Mo <sub>0.2</sub> C	0.444*	N/A	0.02	0.02	≤10, spherical
	Ti <sub>0.74</sub> Nb <sub>0.26</sub> N	not in XRD	0.07	0.07	N/A	170 to 230
	Ti <sub>0.52</sub> Nb <sub>0.48</sub> C <sub>0.5</sub> N <sub>0.5</sub>	0.4410	0.04	0.04	N/A	60 to 80
	Nb <sub>0.9</sub> Ti <sub>0.1</sub> C <sub>0.5</sub> N <sub>0.5</sub>	0.4450	0.06	0.06	N/A	25 to 70
X80-B4F	Nb <sub>0.68</sub> Mo <sub>0.32</sub> C	0.442*	N/A	0.05	0.05	≤10, spherical
	Ti <sub>0.72</sub> Nb <sub>0.28</sub> N	0.4302	0.03	0.03	N/A	80 to 100
	Nb <sub>0.57</sub> Ti <sub>0.43</sub> C <sub>0.5</sub> N <sub>0.5</sub>	0.4384	0.10	0.10	N/A	85 to 135
	Nb <sub>0.92</sub> Ti <sub>0.08</sub> C <sub>0.5</sub> N <sub>0.5</sub>	0.4446	0.06	0.06	N/A	40 to 100
X80-A4F	Nb <sub>0.78</sub> Mo <sub>0.22</sub> C	0.444*	N/A	0.06	0.06	≤10, spherical
	Ti <sub>0.75</sub> Nb <sub>0.25</sub> N	0.4293	0.09	0.09	N/A	100 to 200
	Nb <sub>0.51</sub> Ti <sub>0.49</sub> C <sub>0.5</sub> N <sub>0.5</sub>	0.4399	0.10	0.10	N/A	20 to 30
	Nb <sub>0.86</sub> Ti <sub>0.14</sub> C <sub>0.5</sub> N <sub>0.5</sub>	0.4430	0.11	0.11	N/A	20 to 30
	Nb <sub>0.74</sub> Mo <sub>0.26</sub> C	0.443*	N/A	0.03	0.03	≤10, spherical

N/A, not applicable.

Not in XRD: The precipitates were observed by TEM, however, because of the small amounts were not detected in the XRD pattern.

\*Lattice parameters for the nanoprecipitates were obtained from electron diffraction patterns.

(≤10 nm, Nb/Mo-rich) were identified.<sup>[10]</sup> The classification criterion was based on precipitate solubilities (Figure 2) as explained subsequently. Few large, Ti-rich precipitates (500 to 3000 nm) were found in the X70 and X80 steels compared with the Grade100 steel. For the X80-462, X80-B4F, and X80-A4F steels, Ti-rich precipitates were observed with sizes of approximately 100 to 200 nm. They were formed at higher rolling temperatures and are expected to contain little or no C, so to simplify analysis the composition is listed as (Ti,Nb)N. For all steels, Ti/Nb-rich and Nb-rich precipitates with sizes of approximately 30 to 60 nm are expected to form at lower rolling temperatures. These contain both C and N. To simplify the calculations (at least initially), the C and N amounts were assumed to be similar. (The actual compositions could vary somewhat from this simplifying assumption.) A small amount of Mo was detected in the larger precipitates from the X70-564 steel. Compared with the other precipitates, Mo carbides have the highest solubility.<sup>[15,16]</sup> The precipitation of Mo indicates that its solubility limit has been reached.

As shown in Table IV, nanoprecipitates (mostly ≤10 nm) were identified in Grade100, X70, and X80 steels. They form at lower temperatures during or after coiling and are expected to be carbides. They are Nb-rich with significant amounts of Mo. Some chemistry

**Table V. Lattice Parameters for Binary Carbides and Nitrides<sup>[17]</sup>**

Lattice Parameter (nm)	TiN	TiC	NbN	NbC
a	0.42417	0.43274	0.43927	0.44698

variations (Nb and Mo) occur for the different steels. The size and chemistry differences between the various precipitates are caused by a variation in the nucleation temperature, nucleation time, and steel compositions. Molybdenum is identified only in the nanoprecipitates (≤10 nm) for most steels, except for the X70-564 steel. This means that, with the exception of the X70-564 steel, the Mo present in precipitate form is only in the nanoprecipitates; this finding is used later in this article to determine the amount of nanoprecipitates.

Calculations were performed to determine whether the lattice parameters for the Ti/Nb carbonitrides (column 3 of Table IV, determined from Rietveld refinement) correlated with the compositions obtained from TEM analysis (column 2 of Table IV). Lattice parameters for binary Ti and Nb carbides and nitrides are shown in Table V; these were obtained from the International Center for Diffraction Database.<sup>[17]</sup>



Because the binary precipitates all have the same crystal structure with similar lattice parameters, it is reasonable to assume that the lattice parameters for the ternary phases (Ti/Nb carbides and Ti/Nb nitrides) or Ti/Nb carbonitrides can be estimated by linear interpolation between the appropriate binary phases. For example, the lattice parameter for  $Ti_xNb_{1-x}N$  can be calculated by linearly interpolating between the lattice parameters for TiN and NbN for the desired value of  $x$ . This process can be used in reverse, *i.e.*, the composition of a particular precipitate can be determined if its lattice parameter is known.

These calculations were done using the lattice parameters for the precipitates from Grade100 and two X80 steels in Table IV. The nanoprecipitates were excluded because of the compositional complexity (four transition metal components for nanoprecipitates from Grade100) or the lack of a lattice parameter for MoC. Two assumptions were made. The first precipitate from Grade100 and X80 steels in Table IV was assumed to be a nitride (no carbon) to determine the Ti and Nb compositions. This assumption is reasonable as it is the largest precipitate, forms at the highest temperature, and as such, is expected to contain little or no C. The other precipitates were assumed to be carbonitrides. The Ti and Nb compositions, which were obtained from a TEM analysis, were taken as correct, so that the C and N compositions could be determined. Note that in

Table IV, the C and N amounts were assumed to be 0.5 in the precipitate formulae because the C and N compositions could not be determined from EDX analysis. The resultant precipitate compositions are shown in Table VI.

The first precipitate (Ti/Nb nitride) from the Grade100 and X80 steels in the table shows good agreement with the composition obtained from TEM-EDX analysis (Column 2 of Table IV). For the other precipitates, the relative N and C compositions show the correct trend, *i.e.*, the C amount increases as the precipitates become more Nb-rich (Ti-deficient).

Similarly, the precipitates were characterized for the three X100 steels. Table VII shows the precipitate groupings from the three X100 steels according to the chemistry and size, where the average composition, composition range (standard deviation), and size of the precipitates are shown.

Because of the higher V content in the X100-2B steel, a small amount of V was identified in all precipitates in the X100-2B steel. However, Mo was not identified in the precipitates from X100-2B steel, which is consistent with the ICP results (Table III). Finer precipitates, less than 10 nm in size, were not observed in these three X100 steels. This might be because of the different processing histories and will be discussed subsequently. The precipitates in the X100 steels are relatively small (less than 100 nm) compared with the precipitates

**Table VI. Precipitate Chemistry Calculations for Grade100 and Two X80 Steels**

Steel	Mean Precipitate Chemistry from TEM-EDX	C and N Content Calculations
Grade100	Ti <sub>0.9</sub> Nb <sub>0.1</sub> N Ti <sub>0.77</sub> Nb <sub>0.23</sub> C <sub>0.5</sub> N <sub>0.5</sub> Ti <sub>0.5</sub> Nb <sub>0.5</sub> C <sub>0.5</sub> N <sub>0.5</sub> Nb <sub>0.7</sub> Ti <sub>0.3</sub> C <sub>0.5</sub> N <sub>0.5</sub> Nb <sub>0.48</sub> Mo <sub>0.28</sub> Ti <sub>0.21</sub> V <sub>0.03</sub> C	Ti <sub>0.95</sub> Nb <sub>0.05</sub> N Ti <sub>0.77</sub> Nb <sub>0.23</sub> C <sub>0.07</sub> N <sub>0.93</sub> Ti <sub>0.5</sub> Nb <sub>0.5</sub> C <sub>0.14</sub> N <sub>0.86</sub> Nb <sub>0.7</sub> Ti <sub>0.3</sub> C <sub>0.90</sub> N <sub>0.10</sub> N/A
X80-462	Ti <sub>0.76</sub> Nb <sub>0.24</sub> N Ti <sub>0.55</sub> Nb <sub>0.45</sub> C <sub>0.5</sub> N <sub>0.5</sub> Nb <sub>0.86</sub> Ti <sub>0.14</sub> C <sub>0.5</sub> N <sub>0.5</sub> Nb <sub>0.8</sub> Mo <sub>0.2</sub> C	Ti <sub>0.87</sub> Nb <sub>0.13</sub> N Ti <sub>0.55</sub> Nb <sub>0.45</sub> C <sub>0.32</sub> N <sub>0.68</sub> Nb <sub>0.86</sub> Ti <sub>0.14</sub> C <sub>0.80</sub> N <sub>0.20</sub> N/A
X80-B4F	Ti <sub>0.72</sub> Nb <sub>0.28</sub> N Nb <sub>0.57</sub> Ti <sub>0.43</sub> C <sub>0.5</sub> N <sub>0.5</sub> Nb <sub>0.92</sub> Ti <sub>0.08</sub> C <sub>0.5</sub> N <sub>0.5</sub> Nb <sub>0.78</sub> Mo <sub>0.22</sub> C	Ti <sub>0.60</sub> Nb <sub>0.40</sub> N Nb <sub>0.57</sub> Ti <sub>0.43</sub> C <sub>0.7</sub> N <sub>0.3</sub> Nb <sub>0.92</sub> Ti <sub>0.08</sub> C <sub>0.84</sub> N <sub>0.16</sub> N/A

**Table VII. Classification of Precipitates for X100-A, X100-2B, and X100-3C Steels According to Composition and Size Range (from TEM)**

Steel	Mean Precipitate Chemistry	Lattice Parameter (nm)	Standard Deviation of Composition in Atomic Fraction				Size (nm)
			Ti	Nb	Mo	V	
X100-2A	Ti <sub>0.70</sub> Nb <sub>0.26</sub> Mo <sub>0.04</sub> C <sub>0.5</sub> N <sub>0.5</sub>	0.4339	0.05	0.05	0.02	N/A	30 to 40
	Ti <sub>0.54</sub> Nb <sub>0.41</sub> Mo <sub>0.05</sub> C <sub>0.5</sub> N <sub>0.5</sub>	0.4425	0.04	0.04	0.02	N/A	20 to 30
X100-2B	Ti <sub>0.66</sub> Nb <sub>0.29</sub> V <sub>0.05</sub> C <sub>0.5</sub> N <sub>0.5</sub>	0.4317	0.07	0.06	N/A	0.01	40 to 80
	Nb <sub>0.53</sub> Ti <sub>0.42</sub> V <sub>0.05</sub> C <sub>0.5</sub> N <sub>0.5</sub>	0.4431	0.1	0.11	N/A	0.02	30 to 50
	Nb <sub>0.85</sub> Ti <sub>0.13</sub> V <sub>0.02</sub> C <sub>0.5</sub> N <sub>0.5</sub>	0.4447	0.06	0.07	N/A	0.01	40 to 55
X100-3C	Ti <sub>0.50</sub> Nb <sub>0.47</sub> Mo <sub>0.03</sub> C <sub>0.5</sub> N <sub>0.5</sub>	0.4254	0.06	0.06	0.01	N/A	20 to 40
	Nb <sub>0.67</sub> Ti <sub>0.3</sub> Mo <sub>0.03</sub> C <sub>0.5</sub> N <sub>0.5</sub>	0.4415	0.07	0.08	0.01	N/A	20 to 30



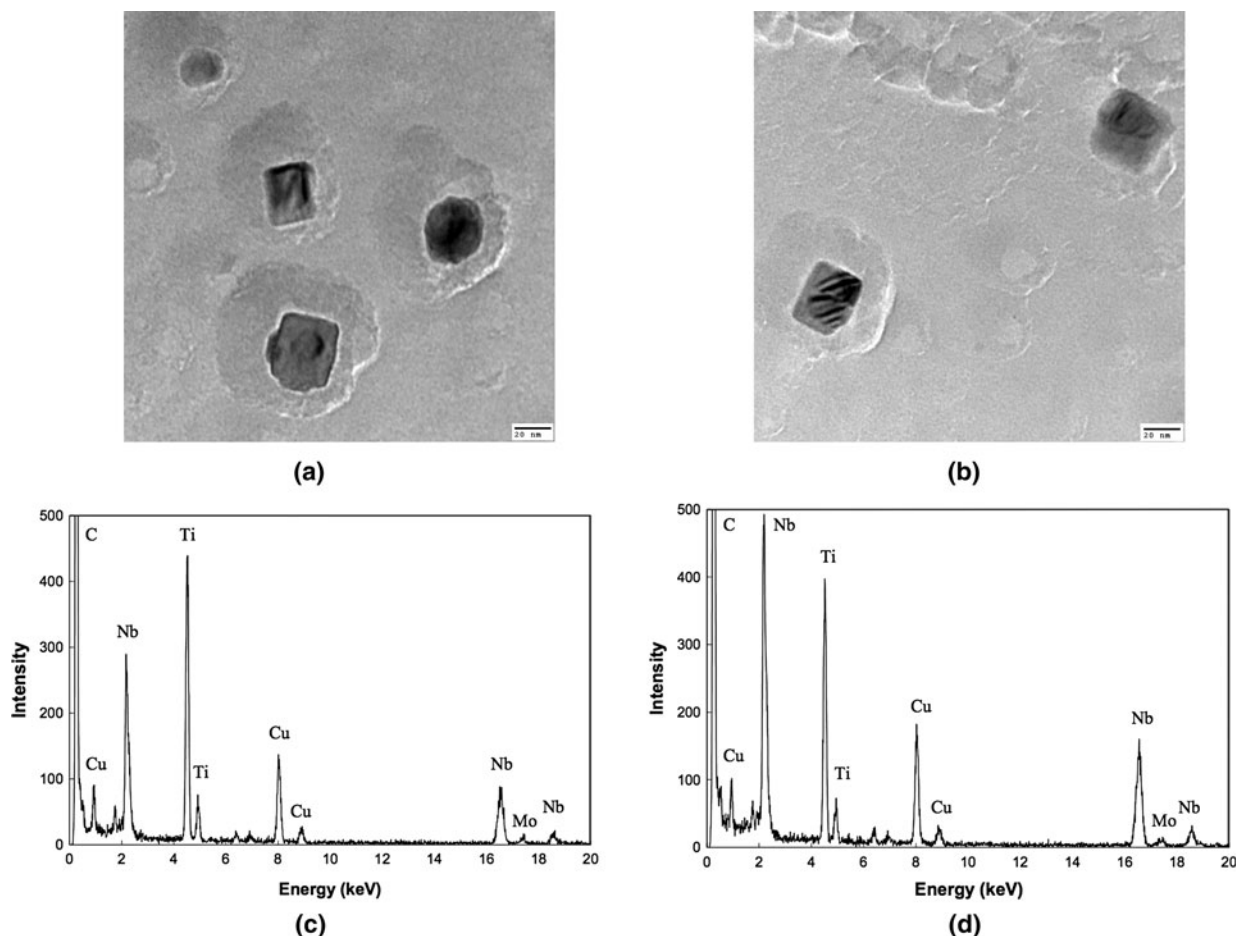


Fig. 6—TEM BF images and EDX spectra of precipitates extracted from X100-2A steel by carbon replicas: (a, b) TEM BF images and (c, d) EDX spectra from precipitates 1 and 2 in (b).

formed at high temperatures in other steels. Figure 6 shows two TEM images and the EDX spectra of the precipitates from the X100-2A steel. The C and N amounts were assumed to be 0.5 in the precipitate formulae in all three X100 steels. The precipitates from the X100 steels were excluded for C/N calculations because of the compositional complexity (three transition metal components).

#### D. Size Distribution of Nanoprecipitates ( $\leq 10$ nm) from Different Steels

As mentioned, the size distribution of the nanoprecipitates was investigated using DF images via carbon replicas. Figure 7 shows an example of a TEM bright-field (BF) image (Figure 7(a)), a DF image (Figure 7(b)), and an EDX spectrum (Figure 7(c)) of nanoprecipitates from the X80-462 steel. An SAD pattern from the field of view is also shown in the inset of Figure 7(a). The fine precipitates have a NaCl-type crystal structure, and the DF image was taken using part of the  $\{111\}$  and  $\{200\}$  diffraction rings. The EDX spectrum shows that the nanoprecipitates are Nb- and Mo-rich. The size distributions for the nanoprecipitates in the X70, X80, and Grade100 steels are slightly different, and a comparison of the cumulative distributions of nanoprecipitates is shown in Figure 8.

Figure 9 shows the effect of normalized CT/ICT temperature on the size (both mode and median) of the nanoprecipitates. The mode is defined as the precipitate size at the peak position in the relative frequency distribution<sup>[10]</sup> (Figure 4(d) in Reference 7). The median size is the size at 50 pct along the  $y$  axis in the cumulative distribution curve (Figure 8). The median size is slightly larger than the mode size for the preceding steels. The X80-A4F steel has the finest nanoprecipitates. The nanoprecipitates in the X80-462 and X80-A4B steels are slightly larger than for X80-A4F. The nanoprecipitates in the X80-B4F and Grade100 steels lie between the two sizes. Neither the mode nor the median of the nanoprecipitates shows a strong relationship with the CT/ICT temperature because of the similar CT/ICT values (0.9 to 1.09 normalized CT/ICT).

#### E. XRD Analysis of Extracted Residues and Rietveld Refinement of the XRD Data

Because the crystal structure (NaCl-type) and lattice parameters of the precipitates are similar and the lattice parameters vary with composition, it is difficult to differentiate between the various carbides, nitrides, and carbonitrides. The XRD patterns from extracted residues were obtained for all steels; Figure 10 shows patterns from four of these steels (Grade 100, X70-564,

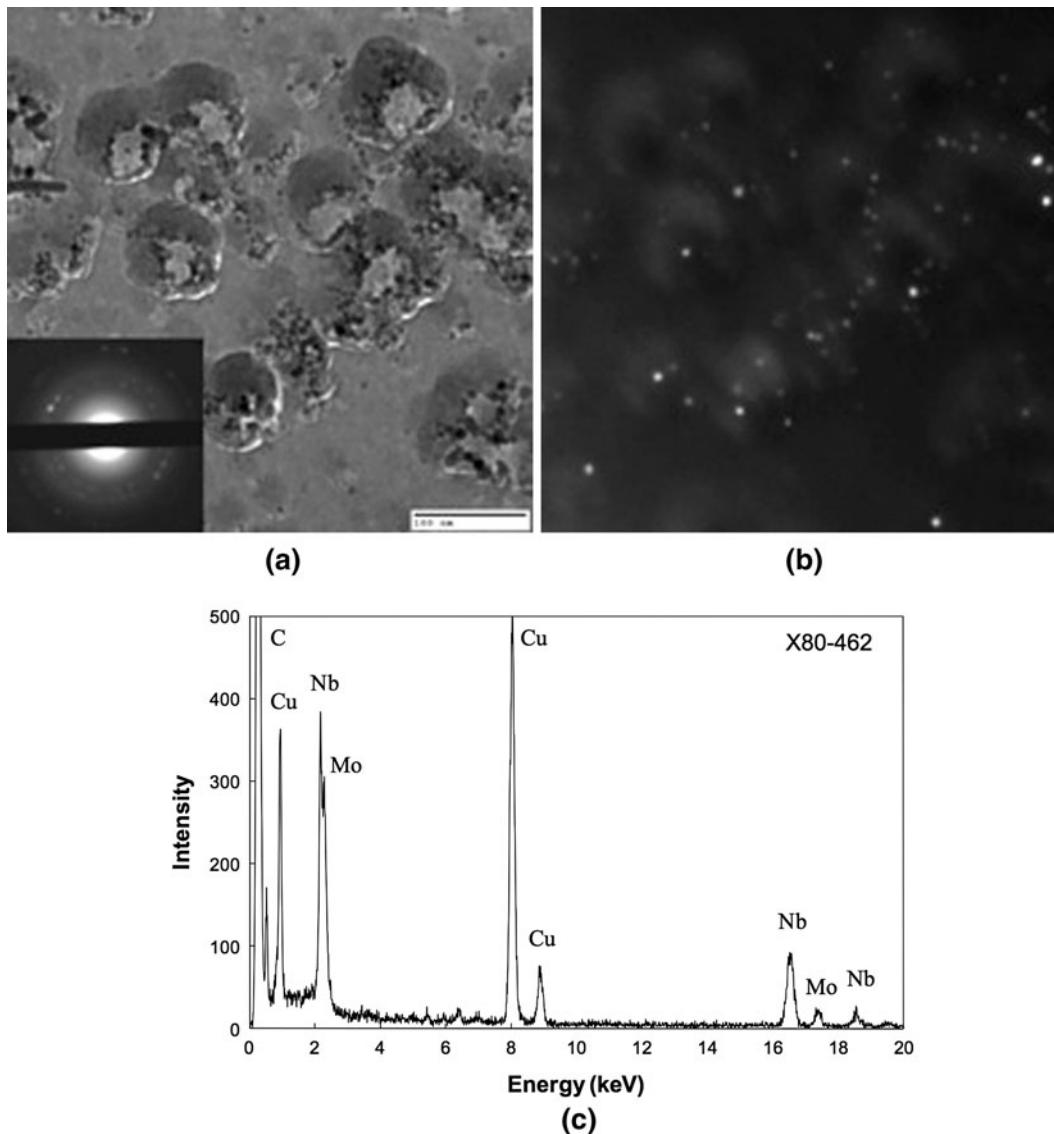


Fig. 7—(a) TEM BF image of nanoprecipitates ( $\leq 10$  nm) extracted *via* a carbon replica from X80-462 steel. The inset in (a) shows the corresponding SAD pattern from the field of view, indicating that the fine precipitates have a NaCl-type crystal structure. (b) TEM DF image, taken using part of the  $\{111\}$  and  $\{200\}$  diffraction rings, of the same area shown in (a). (c) EDX spectrum from several nanoprecipitates shown in (a). The Cu peak in the EDX spectrum is from the support grid.

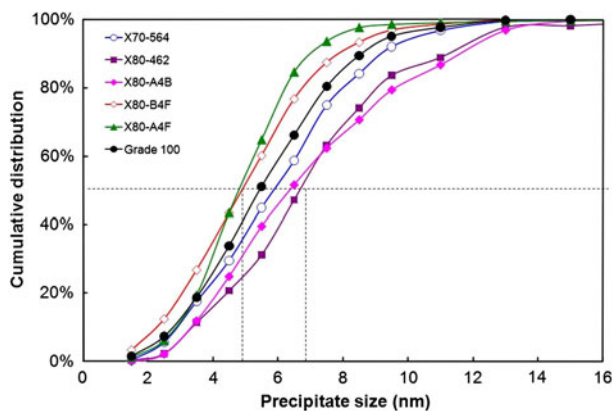


Fig. 8—Cumulative distribution of nanoprecipitates (mainly  $\leq 10$  nm) in different steels.

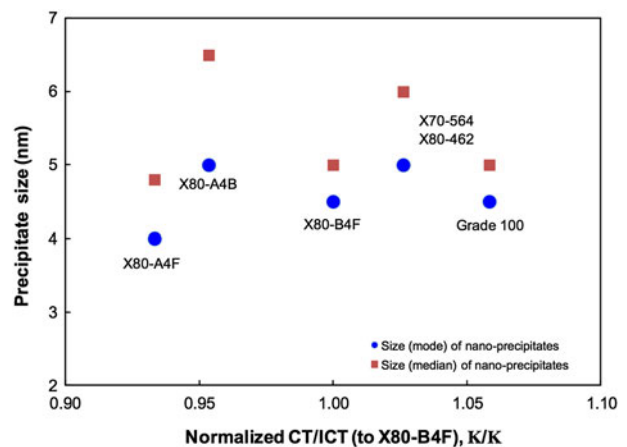


Fig. 9—Effect of CT/ICT on the sizes (both mode and median) of nanoprecipitates (mainly  $\leq 10$  nm).

X80-462, and X100-2A). A broad peak, between the  $2\theta$  angles of 20 deg and 30 deg, is observed for the residues from all steels. The peak is caused by the presence of amorphous silica, which forms during the HCl dissolution process. A preliminary analysis of the diffraction patterns seems to show either one (X70-564) or two crystalline phases with similar NaCl-type structures. One set of peaks (indicated by squares in Figure 10) has smaller  $d$ -spacings, and the other set (more intense peaks—circles in Figure 10) has larger  $d$ -spacings.

A detailed analysis of the XRD patterns was done via Rietveld refinement. This method has been described in detail previously for a Grade100 steel,<sup>[10]</sup> and the same procedure was applied to the steels in this work. Because of the peak overlap between the nanoprecipitates and amorphous SiO<sub>2</sub>, these two phases were considered together as one phase in the Rietveld refinement. SiO<sub>2</sub> was used as an internal standard, and the resulting residual amorphous content was ascribed to the nanoprecipitates. The amount of the SiO<sub>2</sub> was determined from the Si content in the residue, *i.e.*, the total amount of Si in the steel minus the amount in the supernatant (Table III, ICP analysis). To apply Rietveld refinement to the amorphous SiO<sub>2</sub> structure, a crystalline form of silica, cristobalite, was used to approximate the amorphous phase. Cristobalite has a tetragonal structure

( $a = 0.49732$  nm and  $c = 0.69236$  nm).<sup>[17]</sup> It has the same composition and similar  $d$ -spacings as the amorphous SiO<sub>2</sub>.<sup>[10]</sup>

## IV. DISCUSSION

### A. Determination of Relative Abundance of Nanoprecipitates in Steels

The relative abundance (expressed as wt pct) of the constituent crystalline phases in the extracted residues was determined from Eq. [2], where the scale factors, which are determined by the mass, number, and volume of the unit cell of each phase, are derived from Rietveld refinement of the XRD data. According to the experimental extraction yield, the relative wt pct of the crystalline phases to the amount of steel can be obtained. Because the nanoprecipitates ( $\leq 10$  nm) are the focus of this study, the relative wt pct of the nanoprecipitates in the extracted residue (for all the steels with nanoprecipitates) determined from Rietveld refinement is shown in Table VIII.

As mentioned, the amount of nanoprecipitates ( $\leq 10$  nm) can be determined based on the Mo content as well. ICP analysis of the supernatant (Table III) indicates that most of the Mo is present in solid solution in the ferrite. The remaining Mo (with the exception of the X100 steels, which had no nanoprecipitates, and the X70-564 steel) is present only in the nanoprecipitates ( $\leq 10$  nm), as confirmed by TEM-EDX analysis (Table IV). Therefore, the amount of nanoprecipitates ( $\leq 10$  nm) can be determined using Eq. [3]. This is based on the chemistry of the nanoprecipitates and the total amount of Mo available for precipitation. For the X70-564 steel, because only minor amounts of Mo were found in the other precipitates, it was assumed for simplicity that any Mo in precipitates was only in the nanoprecipitates.

$$\frac{wt_{Mo}}{A_{Mo}} = \frac{wt_{ppt}}{A_{ppt}} \times \text{at. fraction}_{Mo} \quad [3]$$

where  $wt_{Mo}$  is the total amount (weight) of Mo available for precipitation, which was determined from the total amount of Mo in the steel minus that in the supernatant via ICP analysis;  $wt_{ppt}$  is the amount (weight) of

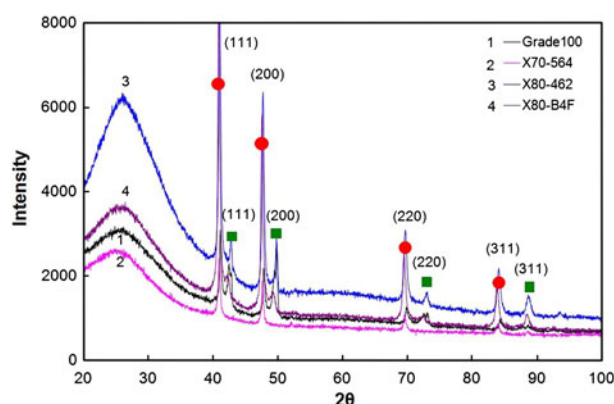


Fig. 10—XRD patterns for residues extracted from different steels by chemical dissolution (HCl).

**Table VIII. Weight Fraction, Volume Fraction, Number Density and Strengthening Effect of Nanoprecipitates (Mainly  $\leq 10$  nm) in the Steels**

Steel	Phases	Weight Fraction (wt pct)	Volume Fraction (vol pct)	Diameter with the Largest Number Distribution (nm)	Number Density (# per $\mu\text{m}^3$ )	Precipitation Strengthening ( $\sigma_{ppt}$ ) (MPa)
Grade100	Nb <sub>0.48</sub> Mo <sub>0.28</sub> Ti <sub>0.21</sub> V <sub>0.03</sub> C	0.157	0.166	4.5	34770	195.0
X70-564	Nb <sub>0.58</sub> Mo <sub>0.42</sub> C	0.092	0.087	5	13299	133.8
X80-462	Nb <sub>0.8</sub> Mo <sub>0.2</sub> C	0.118	0.116	5	17671	154.2
X80-A4B	Nb <sub>0.68</sub> Mo <sub>0.32</sub> C	0.107	0.104	5	15862	146.1
X80-B4F	Nb <sub>0.78</sub> Mo <sub>0.22</sub> C	0.116	0.114	4.5	23911	161.7
X80-A4F	Nb <sub>0.76</sub> Mo <sub>0.24</sub> C	0.035	0.034	4	10121	93.3
X100-2A	N/A	0	0	—	0	—
X100-2B	N/A	0	0	—	0	—
X100-3C	N/A	0	0	—	0	—



nanoprecipitates ( $\leq 10$  nm), to be determined;  $A_{\text{Mo}}$  is the atomic weight of Mo;  $A_{\text{ppt}}$  is the molecular weight of the nanoprecipitates ( $\leq 10$  nm); and  $\text{at. fraction}_{\text{Mo}}$  is the atomic fraction of Mo in the nanoprecipitates ( $\leq 10$  nm), from the nanoprecipitate composition determined from a TEM-EDX microanalysis.

Figure 11 shows a comparison of the amount of nanoprecipitates in the X70, X80, and Grade 100 steels. The results are calculated based on Rietveld refinement of the XRD patterns from the extracted residues and based on the Mo amount determined from an ICP analysis. The amounts of nanoprecipitates ( $\leq 10$  nm) determined by the two methods are similar for the same steel.

### B. Determination of Volume Fraction and Number Density of Nanoprecipitates in Steels

The volume fraction and number density of the nanoprecipitates ( $\leq 10$  nm) can be determined from their weight fraction, which has been explained previously. The nanoprecipitates have a NaCl-type structure. From the precipitate chemistry, the density of the precipitates can be expressed mathematically as follows<sup>[18]</sup>:

$$\rho_{\text{ppt}} = \frac{nA_{\text{ppt}}}{VN_A} \quad [4]$$

where  $\rho_{\text{ppt}}$  is the density of the nanoprecipitate,  $n$  is the number of formula units in the unit cell ( $n = 4$ ),  $A_{\text{ppt}}$  is the molecular weight of the precipitate,  $V$  is the volume of the unit cell ( $V = a^3$ , where  $a$  is the lattice parameter of the nanoprecipitate), and  $N_A$  is Avogadro's number ( $6.023 \times 10^{23}$  atoms/mol).

The molecular weight  $A_{\text{ppt}}$  can be calculated from the following equation, using  $\text{Nb}_x\text{Mo}_y\text{C}$  as an example:

$$A_{\text{ppt}} = A_{\text{Nb}} \times X + A_{\text{Mo}} \times Y + A_{\text{C}} \quad [5]$$

where  $A_{\text{ppt}}$  is the molecular weight of the precipitate,  $A_{\text{Nb}}$  is the atomic weight of Nb,  $A_{\text{Mo}}$  is the atomic weight of Mo,  $A_{\text{C}}$  is the atomic weight of C,  $X$  is the atomic fraction of Nb, and  $Y$  is the atomic fraction of Mo.

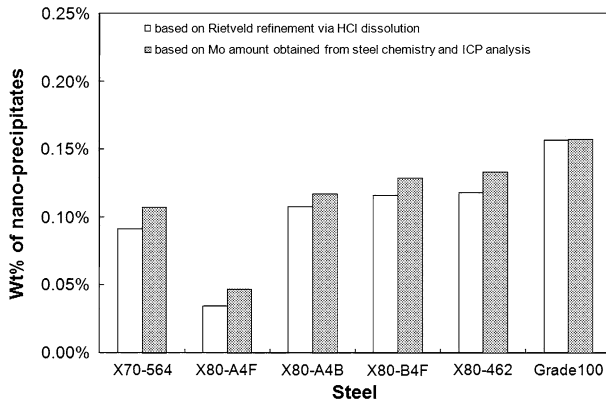


Fig. 11—Relative amount of nanoprecipitates ( $\leq 10$  nm) compared with the original weight of the steel.

The volume fraction of the nanoprecipitates ( $\leq 10$  nm) can be calculated as:

$$\text{vol fraction}_{\text{ppt}} = \frac{\text{wt fraction}_{\text{ppt}} \times \rho_{\text{Fe}}}{\rho_{\text{ppt}}} \quad [6]$$

where  $\text{vol fraction}_{\text{ppt}}$  is the volume fraction of the nanoprecipitates in one unit volume of steel,  $\rho_{\text{Fe}}$  is the density of Fe ( $\sim 7.87$  g/cm<sup>3</sup>),<sup>[18]</sup>  $\rho_{\text{ppt}}$  is the density of nanoprecipitates, and  $\text{wt fraction}_{\text{ppt}}$  is the weight fraction of the nanoprecipitates.

From the preceding TEM precipitate characterization, the nanoprecipitate diameter with the largest number distribution is listed in Table VIII (obtained from Figure 8). Assuming all the nanoprecipitates ( $\leq 10$  nm) are spherical with radius  $r$ , the volume of a single precipitate can be expressed as

$$\text{Vol}_{\text{single}} = \frac{4\pi r^3}{3} \quad [7]$$

The number density of the nanoprecipitates in one unit volume of steel can be calculated based on the total volume of the nanoprecipitates and the volume of a single precipitate, which can be expressed as:

$$\# \text{ density} = \frac{\text{Vol}_{\text{ppt}}}{\text{Vol}_{\text{single}}} \quad [8]$$

where  $\text{Vol}_{\text{ppt}}$  is the total volume of nanoprecipitates in 1  $\mu\text{m}^3$  of steel,  $\text{Vol}_{\text{single}}$  is the volume of a single nanoprecipitate, and  $r$  is the radius of nanoprecipitate ( $\leq 10$  nm) with the largest number distribution determined by DF imaging.

The weight fraction, volume fraction, and number density of the nanoprecipitates ( $\leq 10$  nm) for different steels, extracted by HCl dissolution, are shown in Table VIII. No nanoprecipitates were observed in the X100 steels. The volume fraction and number densities are summarized in Figure 12; both exhibit the same trend. Grade100 has the highest amount of nanoprecipitates, whereas X80-A4F has the lowest amount. The Grade100, X70, and X80 steels all had similar processing histories, so processing is not responsible directly for the differences. The amount of nanoprecipitates may be related to the amount of Nb because Nb is the main component in the nanoprecipitates. The lack of nanoprecipitates for X100 steels is caused by the low ICT temperature, which will be discussed in the next section.

### C. Determination of Strengthening Contributions

#### 1. Strengthening component caused by grain refinement

Figure 5 shows a summary of the *m.l.i.* measurements for all steels. Based on this information, the relationship between the strength and the inverse of the square root of the mean linear intercept, i.e.,  $(\text{m.l.i.})^{-1/2}$ , is plotted in Figure 13. Both the adjusted and unadjusted values are plotted. The unadjusted values are based simply on the measured values of the yield strength. The adjusted values account for only grain size effects, i.e., the solid

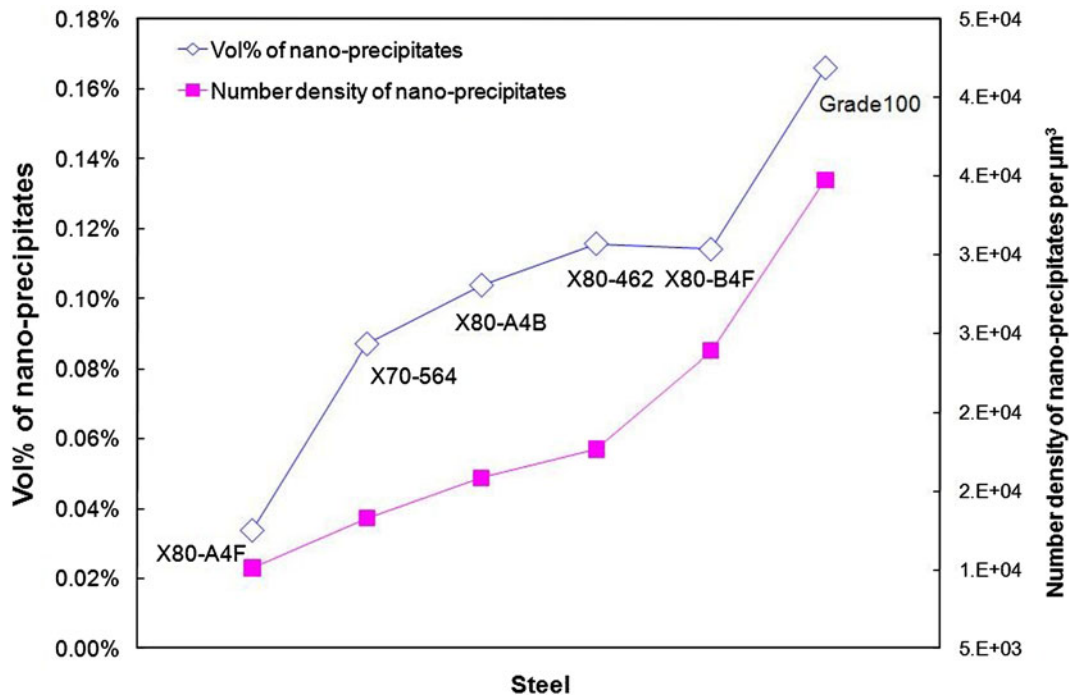


Fig. 12—Volume fraction and number density of nanoprecipitates ( $\leq 10$  nm) per  $\mu\text{m}^3$  in steels (HCl dissolution).

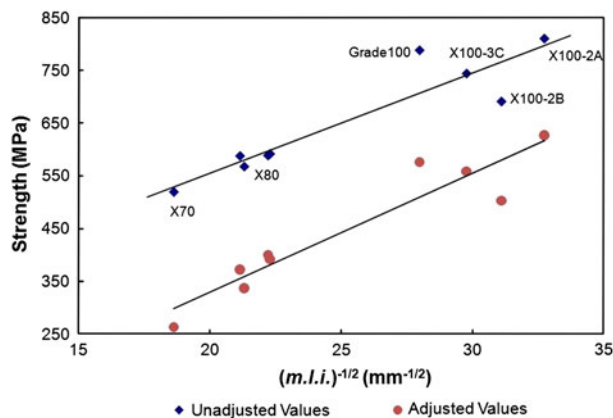


Fig. 13—Relationship between strength and mean linear intercept (mm) for steels studied. Unadjusted values: Yield strength (MPa) =  $19.0 \times (m.l.i.)^{-1/2} + 175.1$ . Adjusted values: Grain size strengthening (MPa) =  $22.6 \times (m.l.i.)^{-1/2} - 122.5$ .

solution, precipitation, and friction stress contributions are excluded; this is discussed in subsequent sections. Reasonable agreement with the Hall-Petch equation is found for both plots. The slopes are similar, with the adjusted plot having a shallower slope. This would suggest that strengthening mechanisms, other than grain size control, are more important for the lower strength grades. Grade100 and X100-2B steels seem to be outliers compared with the other steels. Grade100 is a structural steel with higher C levels and other alloying elements. As such, it could be expected to have a higher precipitation strengthening effect. For the X100-2B steel, the errors may be related to the grain size measurement. As the grains are refined, it becomes increasingly difficult to identify specific grains, which will impact the *m.l.i.* measurements.

The strengthening contribution caused by the grain size was calculated according to Eq. [9], where  $k'_y$  is in the range of 17.5 to 19.2 MPa  $\text{mm}^{1/2}$ . [15]

$$\sigma_{gb} = k_y d^{-1/2} = k'_y (m.l.i.)^{-1/2} \quad [9]$$

where  $\sigma_{gb}$  is the grain boundary strengthening,  $k_y$  is the strengthening coefficient when grain size ( $d$ ) is used, and  $k'_y$  is the strengthening coefficient when the mean linear intercept (*m.l.i.*) is used.

The grain size strengthening component is between 336.9 and 592.4 MPa for the steels studied. The X70-564 steel has the largest grain size and the lowest grain size strengthening effect. Alternatively, the X100 steels have the smallest grain sizes and the greatest grain size strengthening effects.

In TMCP, it is expected that the processing histories, such as the accelerated cooling (CR) and coiling temperature or interrupted cooling temperature, will affect the steel microstructure evolution. Figure 14 shows the effect of CR on the *m.l.i.* of the steels, which indicates that the grain size decreases with an increase in the steel grade. Because only the nominal CR values are available for X70, X80, and Grade100 steels, and they are the same, there is no point to discussing the effect of CR on the *m.l.i.* for these steels. However, a significant change in grain size for these steels is observed. For the X100 steels, a significant change in CR is observed between X100-3C and the other two steels (X100-2A and X100-2B), but their grain sizes are almost the same. This finding indicates that the steel microstructure evolution and/or other factors (*e.g.*, steel composition, CT/ICT, rolling conditions, *etc.*) may also contribute to the steel grain size.

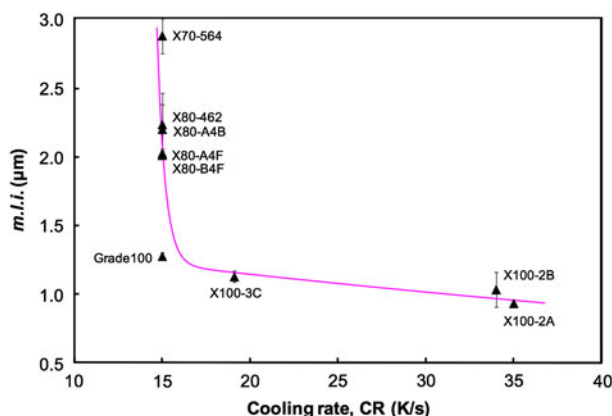


Fig. 14—Effect of CR on mean linear intercept of steels.

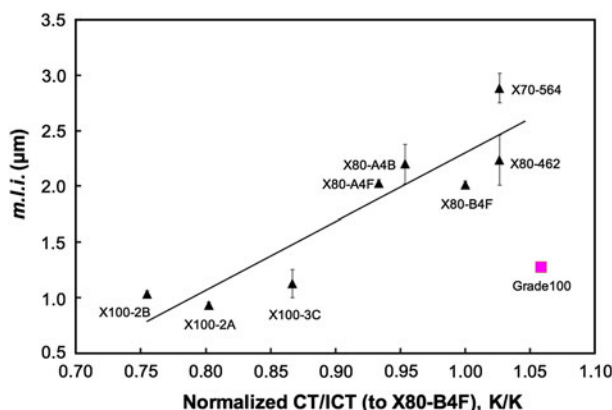


Fig. 15—Effect of CT/ICT on mean linear intercept of steels:  $m.l.i. = 6.2 \times (\text{normalized CT/ICT}) - 3.9$ .

CT/ICT can affect the grain microstructure as well. Figure 15 shows the effect of CT/ICT on the *m.l.i.* of steels. A reasonable linear fit to the data is observed, with the exception of Grade100 steel, which is not included in the linear regression. The strengthening mechanisms for the Grade100 steel are different from the other steels because it is a structural steel with higher amounts of carbon and other alloying elements. However, the other steels are similar in that they are all pipeline grades. The grain size decreases with decreasing CT/ICT, which is consistent with the literature.<sup>[3,19]</sup> This effect is related to the nucleation and grain growth of ferrite during the austenite-to-ferrite transformation. During cooling, the phase transformation is shifted generally to a lower temperature, which is referred to as undercooling. If the steel is cooled quickly, then the undercooling depends on the CT/ICT, with a lower CT/ICT resulting in a higher degree of undercooling. Greater undercooling below  $A_{r1}$  enhances the driving force for the austenite to ferrite transformation, resulting in an increase in the ferrite nucleation rate. As the temperature decreases, the ferrite growth rate is decreased because grain growth is related directly to carbon diffusion out of the austenite. If other processing parameters are the same, then the ferrite nucleation rate increases and grain growth rate decreases at lower

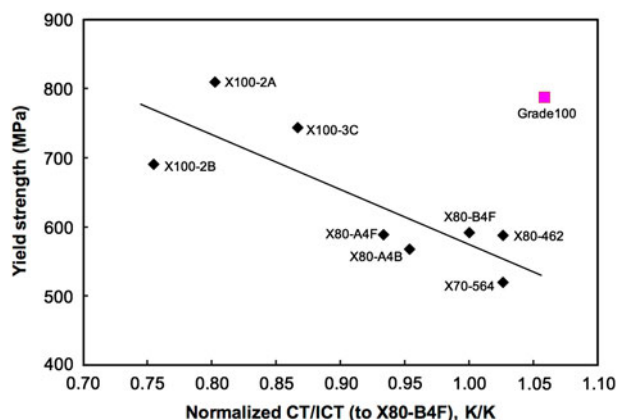


Fig. 16—Effect of CT/ICT on yield strength: Yield strength =  $-796.1 \times (\text{normalized CT/ICT}) + 1370.4$ .

CT/ICT, resulting in a finer ferrite grain size. However, the CT/ICT should not be too low or undesirable low-temperature products such as martensite will form.

Figure 16 shows the effect of CT/ICT on the yield strength of the steels. A reasonable linear fitting is shown as well if Grade 100 is omitted. The yield strength improves with decreasing CT/ICT, which is related to the grain refinement effect discussed in the previous paragraph. If the various grades are considered independently (e.g., X100 and X80 steels), however, then the relationship between yield strength and CT/ICT is less clear. In fact, for the X80 steels, little change in yield strength or grain size (Figure 16) is observed for a normalized CT range of 0.90 to 1.04. This apparent insensitivity to CT may be related to the relatively small temperature range relative to the overall CT/ICT range (0.64 to 1.09) for all the steels. An alternative explanation may be related to the steel chemistry. For example, the X80-A4F and X80-B4F steels have similar compositions with the notable exception of the Nb content—0.077 wt pct for X80-B4F vs 0.044 wt pct for X80-A4F. Niobium can contribute to grain refinement; as such, the higher Nb content in X80-B4F may offset the higher CT (normalized CT = 1.0 for X80-B4F compared with 0.90 for X80-A4F). However, if the X80-462 and X80-A4B steels are compared, the steel compositions are similar (including Nb levels), whereas the normalized CT differs by 0.11. It seems, then, that small changes in CT/ICT have little effect on grain size and yield strength.

From the preceding analysis, a combination of high CR and low CT/ICT in microalloyed steels helps to produce a fine bainitic/acicular ferrite microstructure, making higher strength steels possible.

## 2. Strengthening component caused by solid solution strengthening

The concentrations of the elements present in the supernatant correspond to those dissolved in solid solution in the ferrite. They were analyzed by ICP analysis and include Si, Mn, Cu, Mo, Ni, Cr, Ti, and Nb. Based on the equilibrium solubilities of C and N in ferrite, 0.005 wt pct C<sup>[20]</sup> and 0.01 wt pct N contribute to solid-solution strengthening. Here, supersaturation,



especially for C, is not considered, but is quite possible. Therefore, the following calculations for solid-solution strengthening represent a lower bound solution.

Table IX shows the solid strengthening coefficients and the wt pct of each element in solution.<sup>[15,21–24]</sup>

The solid-solution strengthening was determined according to Eq. [10] with the results shown in Table IX for all steels. The solid-solution strengthening component is between 115 and 163 MPa for the steels studied.

$$\sigma_{ss} = \sum k_i C_i \quad [10]$$

where  $\sigma_{ss}$  is the solid solution strengthening,  $k_i$  is the strengthening coefficient for solute strengthening of solute  $i$ , and  $C_i$  is the concentration of solute  $i$ .

### 3. Strengthening component due to precipitation strengthening

Precipitation strengthening is calculated according to Equation (11), which is based on Orowan looping. An Orowan looping mechanism generally shows an inverse dependence with particle size, and the transition from a cutting mechanism to the Orowan type looping will occur at a small particle size.<sup>[3]</sup> However, direct evidence of the Orowan looping is lacking in this work because of the difficulties in observing such fine precipitates, most of which are only a few nanometers in diameter.<sup>[3]</sup>

$$\sigma_{ppt} = \left( \frac{10.8 f_v^{1/2}}{X} \right) \ln \left( \frac{X}{6.125 \times 10^{-4}} \right) \quad [11]$$

where  $\sigma_{ppt}$  is the precipitation strengthening,  $X$  is the size of precipitates in microns, and  $v_f$  is the volume fraction of a given precipitate size ( $X$ ).

The precipitation strengthening contribution from nanoprecipitates for all the steels studied is shown in Table VIII. For X70, X80, and Grade100 steels, nano-

precipitates (mainly  $\leq 10$  nm) were identified. The volume fraction and the nanoprecipitate diameter with the largest number distribution were used in the calculations. For the X70, X80, and Grade100 steels, precipitation strengthening caused by these nanoprecipitates is between 90 and 195 MPa. The Grade100 steel has the highest volume fraction of nanoprecipitates; therefore, it has the highest precipitation strengthening effect. Alternatively, X80-A4F has the lowest value of precipitation strengthening. No precipitation strengthening effect is found because no nanoprecipitates form ( $\leq 10$  nm) in X100 steels.

In addition to the nanoprecipitates (mainly  $\leq 10$  nm), precipitates larger than 10 nm were identified in the above steels. According to the volume fraction and size of these precipitates, precipitation strengthening (for particles larger than 10 nm and less than 50 nm) can also be calculated using Equation (11), as shown in Table X.

For the X70, X80, and Grade100 steels, nanoprecipitates (mainly  $\leq 10$  nm) contribute to precipitation strengthening. For the X100 steels, the precipitation strengthening contribution is much less compared with other strengthening mechanisms. Table X also indicates that the potential effect of the 10 to 50 nm-size precipitates was not significant.

The Grade100, X70, and X80 steels all have similar processing histories. The amount of nanoprecipitates is related to the amount of microalloying elements. Niobium and Mo, especially Nb, are the main microalloying elements that contribute to the nanoprecipitates ( $\leq 10$  nm). The effect of Nb on the amount of nanoprecipitates in the different grades of steels is shown in Figure 17. Curve fitting using an exponential function is shown as well, although the data from X100 steels are not included because of the absence of nanoprecipitates. For similar processing conditions, a higher Nb content

**Table IX. Solid-Solution Strengthening Contribution in the Steels**

Solute		C	N	Si	Mn	Cu	Mo	Ni	Cr	Ti	Nb
$k_i$ (MPa)		5082	5082	83	31.5	39	11	0	−31	80	2400
Grade 100	wt pct*	0.005	0.0058	0.021	1.541	0.4	0.257	0.259	0.177	0.014	0.003
	$\sigma_{ss}$ (MPa)	125.7									
X70-564	wt pct*	0.005	0.01	0.029	1.341	0.229	0.159	0.116	0.048	0.018	0.013
	$\sigma_{ss}$ (MPa)	163.0									
X80-462	wt pct*	0.005	0.0062	0.019	1.635	0.27	0.273	0.13	0.05	0.007	0.004
	$\sigma_{ss}$ (MPa)	131.2									
X80-A4B	wt pct*	0.005	0.0033	0.017	1.595	0.34	0.271	0.25	0.07	0.002	0.016
	$\sigma_{ss}$ (MPa)	146.7									
X80-B4F	wt pct*	0.005	0.0037	0.017	1.563	0.15	0.273	0.41	0.06	0.003	0.005
	$\sigma_{ss}$ (MPa)	113.8									
X80-A4F	wt pct*	0.005	0.001	0.014	1.704	0.15	0.394	0.41	0.08	0.004	0.009
	$\sigma_{ss}$ (MPa)	115.2									
X100-2A	wt pct*	0.005	0.001	0.02	1.726	0.326	0.407	0.47	0.161	0.007	0.012
	$\sigma_{ss}$ (MPa)	127.6									
X100-2B	wt pct*	0.005	0.0029	0.021	1.728	0.16	0.399	0.439	0.158	0.004	0.013
	$\sigma_{ss}$ (MPa)	132.8									
X100-3C	wt pct*	0.005	0.0029	0.019	1.762	0.15	0.397	0.4	0.163	0.001	0.012
	$\sigma_{ss}$ (MPa)	130.1									

\*wt pct of element in solid solution.

Table X. Strengthening Contributions from Different Mechanisms

Steels	Strengthening Contribution (MPa)						Linear Summation (MPa)	Superposition Using Eq. [12] (MPa)	Actual Yield Strength (MPa)
	$\sigma_i$	$\sigma_{ss}$	$\sigma_{gb}$	$\sigma_{ppt}$		Total			
				≤10 nm	10-50 nm				
Grade100	54	125.7	506.4	195.0	0	195.0	881.0	722.2	788
X70-564	54	163.0	336.9	133.8	17.0	150.8	704.8	586.2	520
X80-462	54	131.2	382.6	154.2	0	154.2	722.0	597.7	588
X80-A4B	54	146.7	385.5	146.1	0	146.1	732.3	613.0	568
X80-B4F	54	113.8	403.3	161.7	0	161.7	732.8	602.3	592
X80-A4F	54	115.2	401.9	93.3	33.8	127.1	698.2	590.7	589
X100-2A	54	127.6	592.4	0	39.1	39.1	813.0	775.3	810
X100-2B	54	132.8	562.8	0	31.3	31.3	780.9	750.5	691
X100-3C	54	130.1	538.8	0	39.2	39.2	762.0	724.3	744

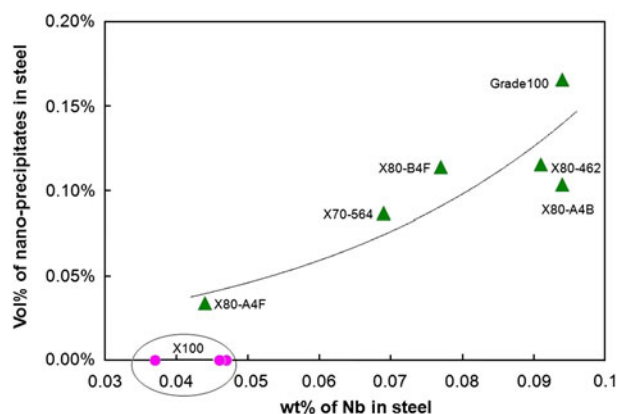


Fig. 17—Effect of Nb content on the amount of nanoprecipitates ( $\leq 10$  nm): Vol pct =  $1.3E-4e^{25.3 \times (\text{wt pct Nb})}$  (Nb content range is 0.044 wt pct – 0.094 wt pct).

leads to increased precipitation, leading to a higher volume fraction.

In the X100 steels, the Nb content is much lower compared with other steels (with the exception of X80-A4F). The Mo content and the (Nb + Mo) content is higher in the X100 steels than the other steels (Table I—again with the exception of X80-A4F). However, nanoprecipitates ( $\leq 10$  nm) were not observed in the X100 steels.

As mentioned previously, Figure 17 shows a general trend for the effect of Nb on the volume fraction of nanoprecipitates. The combined effects of Nb with C and Nb with C and N are also considered in Figure 18. The volume fraction of nanoprecipitates is plotted vs the products of the Nb with C and C/N compositions, *i.e.*, Nb  $\times$  C and Nb  $\times$  (C + N\*) where N\* is the solute N remaining after TiN precipitation assuming all the Ti is tied up as TiN. There is a weak linear relationship, *i.e.*, the volume fraction increases with increasing NbxC or NbxC + N). The nanoprecipitates also contain other microalloying elements such as Ti, V, and most notably Mo, which will affect the volume fraction.

The effect of FRT and CT/ICT on the volume fraction of nanoprecipitates (mainly  $\leq 10$  nm) is shown in Figure 19 and Figure 20, respectively. No obvious relationship was found between FRT and the amount of

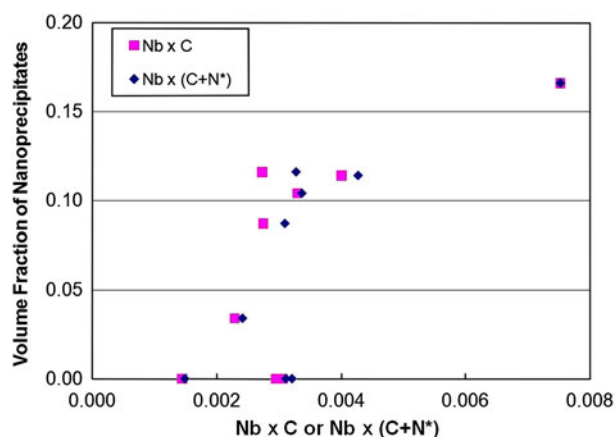


Fig. 18—Effect of Nb  $\times$  C and Nb  $\times$  (C + N\*) on the amount of nanoprecipitates ( $\leq 10$  nm), where N\* is solute N remaining after TiN precipitation.

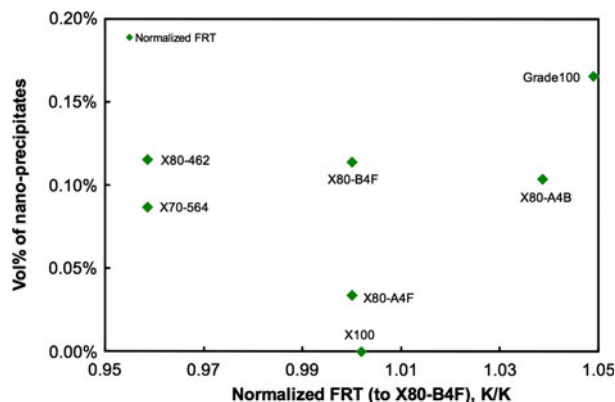


Fig. 19—Volume fraction of nanoprecipitates ( $\leq 10$  nm) as a function of the FRT.

precipitates, which most likely occurs because most nanoprecipitates are formed at lower temperatures, *i.e.*, during or after coiling. However, CT/ICT has a strong effect on nanoprecipitate formation. The relationship between the CT/ICT and the volume fraction of the nanoprecipitates for the X70, X80, and Grade100 steels is fit to a linear relationship as shown in Figure 20,

which indicates that the amount of precipitates increases with increasing CT/ICT. It seems that there is a critical value for CT/ICT (between 0.8 and 0.9, normalized to the ICT for X80-B4F), below which nanoprecipitation does not occur.

Under the same CR conditions, a lower CT/ICT leads to higher undercooling and higher supersaturation of the solutes in ferrite. Thus, a larger driving force for precipitation is generated, which enhances precipitation. However, nucleation is a kinetic process. Insufficient thermal energy exists at low CT/ICT temperatures (<0.9 here), inhibiting the nucleation process. At higher CT/ICT values, the diffusion rates are faster as are the atomic impingement rates, which enhance the nucleation process. However, the driving force is lower and the critical nucleus sizes are larger, which inhibits the number of nuclei present at high temperature. These two competitive processes lead to a maximum precipitation nucleation rate at an intermediate temperature.

CR can affect the precipitation behavior of the nanoprecipitates as well. If CT/ICT is fixed, then a faster CR leads to a higher degree of undercooling and higher supersaturation of the solute (for example Nb) for subsequent precipitation in ferrite. Thus, a larger driving force and higher precipitate nucleation rate can be obtained for precipitation to occur. However, faster cooling of the skelp after the austenite-ferrite transformation may also be translated into lower CT/ICT values, leading to a lower precipitate nucleation rate.

#### 4. Superposition of strengthening mechanisms based on $\sigma_i$ , $\sigma_{ss}$ , $\sigma_{gb}$ and $\sigma_{ppt}$

Based on the above information, the individual strengthening contributions were determined for different steels. The strengthening contribution from the different mechanisms was summarized in Table X. The lattice friction stress for iron ( $\sigma_i$ ) is included as well.<sup>[3]</sup> The superposition of different strengthening contributions is compared with the actual yield strength of the steels in the subsequent text.

If a linear model is used, then the effect of individual strengthening contributions from Peierls-Nabarro barriers, grain boundary strengthening, solid-solution

strengthening, and precipitation strengthening are combined and estimated quantitatively according to Eq. [1].<sup>[3]</sup>

$$\sigma_{ys}(\text{MPa}) = \sigma_i + \sigma_{gb} + \sigma_{ss} + \sigma_{ppt} = \sigma_i + k_y d^{-1/2} + \sum k_i C_i + \sum \left( \frac{10.8 f_v^{1/2}}{X} \right) \ln \left( \frac{X}{6.125 \times 10^{-4}} \right) \quad [1]$$

where  $\sigma_{ys}$  is the yield stress,  $\sigma_i$  is the friction stress of iron,  $\sigma_{gb}$  is the grain boundary strengthening,  $\sigma_{ss}$  is the solid-solution strengthening, and  $\sigma_{ppt}$  is the precipitation strengthening.

Because of the mutual interaction between the grain refinement and precipitation strengthening in microalloyed steel systems,<sup>[25]</sup> a combination of a root mean square and a linear summation model is also used as an alternative. The effect of individual strengthening contributions can be estimated quantitatively by the following equation:

$$\sigma_{ys}(\text{MPa}) = \sigma_i + \sigma_{ss} + \left( \sigma_{gb}^2 + \sigma_{ppt}^2 \right)^{1/2} \quad [12]$$

Table X shows the superposition effect using the two models (2<sup>nd</sup> and 3<sup>rd</sup> last columns), where the four different strengthening components are considered. Figure 21 shows the fitting effect. The experimental yield strength of all the steels sits on a 45 degree line, indicated by circles. Square points in Figure 21 correspond to the yield strength calculated using the linear model. Triangular points correspond to the yield strength calculated using the combination of a root mean square and a linear summation model. It is clear that the yield strength fitting via the combination of root mean square and linear summations is better than that via linear fitting.

If the individual strengthening components are normalized according to the yield strength of the steel, the strengthening contribution for the four different strengthening mechanisms is shown in Figure 22. The figure indicates that strengthening caused by grain size refinement plays a major role for all steels investigated, accounting for as much as 70 pct of the contribution to

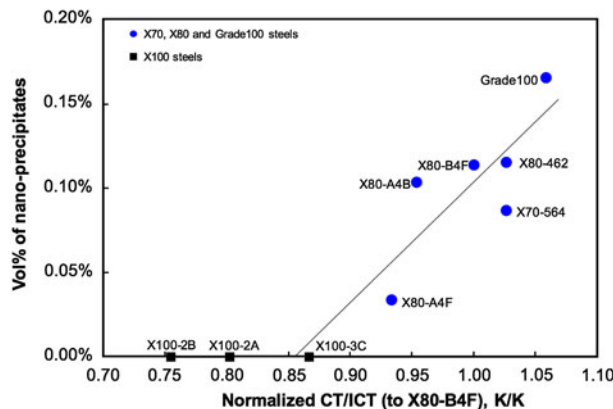


Fig. 20—Effect of CT/ICT on the volume fraction of nanoprecipitates (mainly  $\leq 10$  nm): Vol pct =  $0.007 \times (\text{normalized CT/ICT}) - 0.006$ .

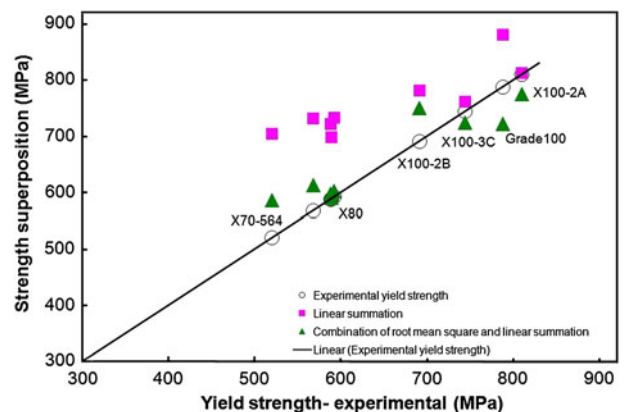


Fig. 21—Superposition of different strengthening components using Eq. [12].



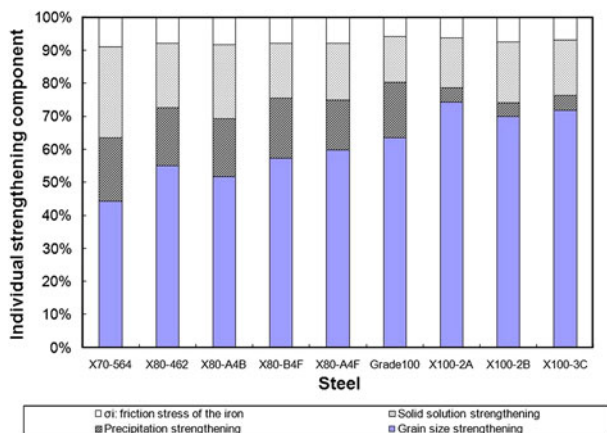


Fig. 22—Individual strengthening components for the steels studied.

the yield strength in the X100 steels. Precipitation and solid solution strengthening account for close to 40 pct of the strengthening in the steels, excluding the X100 steels. This contribution is significant considering the small amount of alloying elements added to the steels. The grain size contribution, as well as the combined effects of the other strengthening contributions, was shown in Figure 13. As indicated previously in Figure 13, grain size control is more prominent relative to other strengthening mechanisms for the higher grade steels (*i.e.*, X100 steels).

## V. CONCLUSIONS

A matrix dissolution technique has been used to extract and quantify the precipitates from a series of microalloyed steels. The following conclusions can be drawn from this investigation:

1. The matrix dissolution method can be successfully used to quantify precipitates in microalloyed steels and can provide valuable quantitative information based on samples that are more representative of the steel strip than only microscopy methods. The volume fraction of nanoprecipitates from the X70, X80, and Grade100 steels varies from 0.034 pct to 0.166 pct (Grade 100 steel).
2. Matrix dissolution and carbon replicas give consistent results regarding the precipitate size and chemistry. Carbon replicas help validate the matrix dissolution technique.
3. Rietveld refinement of XRD patterns can be used successfully to identify and determine the relative amounts of different precipitate phases, making it possible to determine the volume fraction of nanoprecipitates ( $\leq 10$  nm) in microalloyed steels.
4. The grain size decreases with increasing grade of steel and the yield strength follows a Hall-Petch type behavior. Higher cooling rates (CR) and lower coiling temperatures/interrupted cooling temperatures (CT/ICT) promote grain refinement, leading to strength improvement.
5. The nanoprecipitates were observed in the X70, X80, and Grade100 steels. These nanoprecipitates

are generally less than 10 nm in size and spherical in shape. They are mainly Nb-Mo carbides but with chemistry variations. Under similar processing conditions, increasing Nb content leads to a higher yield of nanoprecipitates.

6. For X100 steels, no nanoprecipitates ( $\leq 10$  nm) were observed. The lack of fine precipitates may be due to a combination of low ICT temperature and no coiling.
7. Different strengthening mechanisms contribute to the high strength of microalloyed steels. Each strengthening contribution can be quantified, of which grain refinement plays a major role for the steels being studied accounting for up to 70 pct of the yield strength. Precipitation and solid solution strengthening account for close to 40 pct of the strengthening for all steels, except for the X100 grades.

## ACKNOWLEDGMENTS

The authors thank the Natural Sciences and Engineering Research Council (NSERC) of Canada and Evraz Inc. NA for financial support. Provision of experimental materials by Evraz Inc. NA is gratefully acknowledged.

## REFERENCES

1. D. Bai, M.A. Cooke, J. Asante, and J. Dorricott: Patent U.S. 6,682,613 B2, 2004.
2. S. Wolf: *JOM*, 1967, vol. 19, pp. 22–8.
3. T. Gladman: *The Physical Metallurgy of Microalloyed Steels*, The Institute of Materials, London, U.K., 1997.
4. J. Lu: Ph.D. Dissertation, University of Alberta, Alberta, Canada, 2009.
5. A.J. DeArdo: *Int. Mater. Rev.*, 2003, vol. 48 (6), pp. 371–402.
6. S. Akhlaghi and D.G. Ivey: *Can. Metall. Q.*, 2002, vol. 41 (1), pp. 111–9.
7. Z. Guo and W. Sha: *Mater. Sci. Eng. A*, 2005, vol. 392, pp. 449–52.
8. O. Prat, J. Garcia, D. Rojas, C. Carrasco, and A.R. Kaysser-Pyzalla: *Mater. Sci. Eng. A*, 2010, vol. 572, pp. 5976–83.
9. N. Zavaleta Gutierrez, H. De Cicco, J. Marrero, C.A. Danon, and M.I. Luppó: *Mater. Sci. Eng. A*, 2011, vol. 528, pp. 4019–29.
10. J. Lu, J.B. Wiskel, O. Omotoso, H. Henein, and D.G. Ivey: *Metall. Mater. Trans. A*, 2011, vol. 42A, pp. 1767–84.
11. Internal information, EVRAZ Inc. NA, Regina, Saskatchewan, Canada, September 2008.
12. H.M. Rietveld: *Acta Crystallogr.*, 1967, vol. 22, pp. 151–2.
13. H.M. Rietveld: *J. Appl. Crystallogr.*, 1969, vol. 2, pp. 65–71.
14. J.R. Hill and C.J. Howard: *J. Appl. Crystallogr.*, 1987, vol. 20, pp. 467–74.
15. K. Poorhaydari-Anaraki: Ph.D. Dissertation, University of Alberta, Alberta, Canada, 2005.
16. K.E. Easterling: *Introduction to the Physical Metallurgy of Welding*, Butterworth-Heinemann Ltd, Oxford, U.K., 1992, p. 139.
17. International Center for Diffraction Data (ICDD) database: PDF#00-039-1425, PDF#00-038-1420, PDF#00-032-1383, PDF#00-038-1155, and PDF#00-038-1364.
18. W.D. Callister: *Materials Science and Engineering: An Introduction*, 5th ed., Wiley, New York, NY, 2000, p. 37.
19. V.B. Ginzburg: *Metallurgical Design of Flat Rolled Steels*, Marcel Dekker Inc, New York, NY, 2005.
20. M. Kutz: *Handbook of Materials Selection*, Wiley, New York, NY, 2002, p. 44.

21. D.T. Llewellyn and R.C. Hudd: *Steels: Metallurgy & Applications*, Reed Educational and Professional Publishing Ltd, Oxford, U.K., 1998.
22. J. Heslop and N.J. Petch: *Phil. Mag.*, 1957, vol. 2 (17), pp. 649–58.
23. F.B. Pickering and T. Gladman: *Iron and Steel Institute*, Special report no. 81, 1963, p. 10.
24. P. Buessler, P. Maugis, and O. Bouaziz: *44th Mechanical Working and Steel Processing Conf. Proc.: 8th Int. Rolling Conf. and Int. Symp. on Zinc-Coated Steels*, Iron and Steel Society of AIME, 2002, pp. 1105–16.
25. E. Nembach: *Acta Metall. Mater.*, 1992, vol. 40 (12), pp. 3325–30.

Copyright of Metallurgical & Materials Transactions. Part A is the property of Springer Science & Business Media B.V. and its content may not be copied or emailed to multiple sites or posted to a listserv without the copyright holder's express written permission. However, users may print, download, or email articles for individual use.